

Regularly Spaced Infrared Peaks in the Dusty Spirals of Messier 100

Bruce G. Elmegreen¹, Debra Meloy Elmegreen², Yuri N. Efremov³

ABSTRACT

Spitzer Space Telescope InfraRed Array Camera (IRAC) images of M100 show numerous long filaments with regularly-spaced clumps, suggesting the associated cloud complexes formed by large-scale gravitational instabilities in shocked and accumulated gas. Optical images give no hint of this underlying regularity. The typical spacing between near infrared (NIR) clumps is ~ 410 pc, which is ~ 3 times the clump diameter, consistent with the fastest growing mode in a filament of critical line density. The IRAC magnitudes and colors of several hundred clumps are measured in the most obvious 27 filaments and elsewhere. The clump colors suggest that the dust is associated with diffuse gas, PAH emission, and local heating from star formation. Neighboring clumps on the same filament have similar magnitudes. The existence of many clumps all along the filament lengths suggests that the ages of the filaments are uniform. The observations support a model where interstellar gas is systematically accumulated over lengths exceeding several kpc, forming spiral-like filaments that spontaneously collapse into giant clouds and stellar complexes. Optical wavelengths show primarily the irregular dust debris, HII regions, and lingering star formation downstream from these primal formation sites.

Subject headings: stars: formation — ISM: structure — galaxies: ISM — galaxies: spiral — galaxies: star formation

1. Introduction

Local star formation is often in small filaments that form by transverse compression and then gravitationally collapse in a semi-regular fashion into cores (e.g., André et al 2010;

¹IBM Research Division, T.J. Watson Research Center, 1101 Kitchawan Road, Yorktown Heights, NY 10598; bge@us.ibm.com

²Department of Physics & Astronomy, Vassar College, Poughkeepsie, NY 12604

³Sternberg Astronomical Institute of the Lomonosov Moscow State University, Moscow 119992, Russia

Miettinen 2018). Sometimes these cores are at the intersections of several filaments (Myers 2009). On a galactic scale also, stars form in filaments that may be shock fronts in spiral arms (e.g. Goodman et al. 2014; Ragan et al. 2014) or rings from the expansion of superbubbles (Egorov et al. 2017). Optical observations of galactic-scale star formation is confusing, however, because extinction, irregular morphologies of star complexes, and H α emission that is offset from the gas can make the intrinsic regularities of filament collapse look more chaotic than it is.

Baade (1963) commented that in spiral galaxies, bright stars are “strung out like pearls along the arms.” Early theoretical work considered shock compression (Roberts 1969) and phase transitions (Shu et al. 1972) as a way to enhance gas self-gravity and star formation in the arms. Mouschovias et al. (1974) explained the regular spacing of star formation with a magnetic Rayleigh-Taylor instability. Star formation triggered by enhanced cloud collisions in the arms may also be involved (Kwan & Valdes 1983; Scoville et al. 1986), and even cloud collisions can give a regular spacing because of epicyclic motions (Dobbs 2008c).

To study the regularity of spiral arm star formation in more detail, Elmegreen & Elmegreen (1983) selected 22 galaxies with some evidence for regularity in the optical images and measured the average ratio of the separations to the sizes of the star-forming regions, obtaining a value of 3.1 ± 1.2 . They suggested that the regions formed by gravitational instabilities at the Jeans length for the average gas density and velocity dispersion in the arms. Regularly spaced star-forming clumps were observed more clearly in the spiral arm filaments of the interacting galaxies NGC 2207 and IC 2163 (Elmegreen et al. 2006), where a characteristic luminosity rather than the usual power-law luminosity function was inferred for the regions in the brightest arm. Efremov (2010) measured the properties of regularly spaced star formation in M31, and Gusev & Efremov (2013) observed it in NGC 628. Semi-regular star formation also occurs in nuclear starburst rings (e.g., Pastoriza 1975; Kennicutt et al. 1989; Elmegreen 1994a; Crocker et al. 1996; Comerón et al. 2010; van der Laan et al. 2013; Väisänen et al. 2014), molecular cloud cores (Keto et al. 1991; Sánchez-Monge et al. 2014), debris from interacting galaxies (Wang et al. 2004; Bettoni et al. 2010; Tremblay et al. 2014), and galaxies along Mpc-scale cosmic filaments (Tempel et al. 2014).

Theory suggests that regular fragmentation in filaments is an indication of gravitational instabilities operating at the fastest-growing wavelength (e.g., Inutsuka & Miyama 1992, see Sect. 3 below). Spiral arms filaments presumably differ from local globular filaments (Schneider & Elmegreen 1979). Spiral arms are often modelled as moving through gas over long distances, collecting it into thin dust lanes in what may be a quasi steady-state (Roberts 1969). Other models suggest the filaments are transient (Dobbs & Bonnell 2008a; Dobbs & Pringle 2013), building up until they reach a point of instability, such as a critical line

density, and then collapsing into stars or dispersing by non-linear effects (Chakrabarti et al. 2003).

The earliest theoretical models for gravitational collapse of gas in spiral arms estimated the growth rates and flow-through times and compared the resulting length and mass scales to the available cloud observations (Elmegreen 1979; Cowie 1981; Tomisaka 1987). Early simulations showed the build-up of a magneto-gravitational instability in spiral arms (Kim & Ostriker 2001, 2002) and the important role of gaseous self-gravity in forming giant molecular clouds (Kim & Ostriker 2007). Modern simulations show detailed cloud structure, including regularly-spaced clumps in spiral arms with adaptive mesh gravitational hydrodynamics (Renaud et al. 2013), and highly resolved cloud substructures using particle hydrodynamics with phase transitions (Bonnell et al. 2013), molecule formation (Dobbs et al. 2008b; Duarte-Cabral & Dobbs 2016), and star formation feedback (Dobbs et al. 2011). Simulations also produce filamentary clouds, although in Benincasa et al. (2013) they were irregular with typically one clump per filament, and in Dobbs (2015b) and Duarte-Cabral & Dobbs (2016) they were concentrated in the interarm regions as a result of sheared spiral arm clouds. The observations in the present paper show both arm and interarm filaments and in most cases they contain many clumps with a regularity in their spacing and brightness that is not typically present in simulations (except, e.g., Renaud et al. 2014).

Observations are still unclear about whether spiral arms trigger a net excess of star formation in a galaxy or merely concentrate the gas in the arms, providing the pearls-on-a-necklace appearance without changing the efficiency of star formation per unit gas (Elmegreen & Elmegreen 1986). There is abundant evidence that molecular clouds and star-forming regions are larger in the arms (e.g., Roberts & Stewart 1987; Colombo et al. 2014), but simulations that reproduce this effect do not necessarily have an excess of star formation (Dobbs et al. 2011, 2015a), and the large regions that form can be unbound and easily dispersed in the interarms (Dobbs 2008c). Observations by Koda et al. (2009) support this picture of loose cloud agglomeration and interarm dispersal. A simulation by Baba et al. (2017) also showed that molecular clouds go through the arms with little effect on their internal properties and star formation. Dobbs & Pringle (2009) modelled cloud flow in a spiral arm and reproduced well the Kennicutt-Schmidt relation between the surface densities of star formation and gas, but they also got no enhancement in the specific star formation rate in the arms.

Some observations show that molecular clouds are more self-gravitating in the arms (Hirota et al. 2011), and others show they are not (Donovan Meyer et al. 2013). Shabani et al. (2018) studied spiral arm triggering in a more conventional way, looking for age gradients of star clusters across the arms (Yuan & Grosbol 1981). They found cluster age gradients in

the symmetric two-arm spiral galaxy NGC 1566, but not in M51 or NGC 628, and suggested that M51 has a transient tidal arm rather than a steady wave and NGC 628 is too weak to show a gradient. Another type of transient spiral was modelled by Baba et al. (2013). Transient spirals are not expected to have age gradients because they can accrete gas from both sides (Dobbs & Pringle 2010).

A related observation is of spiral arm spurs or feathers, which can be regular too (Sandage 1961; Lynds 1970; Elmegreen 1980; La Vigne et al. 2006; Puerari et al. 2014). Spurs can arise when the spiral arm condensations driven by self-gravity emerge into the interarms and twist around in a locally reversed shear flow (Balbus 1988; Kim & Ostriker 2002, 2006; Shetty & Ostriker 2006). Shear and other instabilities may contribute too, even without self-gravity (Wada & Koda 2004; Kim et al. 2014, 2015; Dobbs & Bonnell 2006; Sormani et al. 2017). A comprehensive analysis of spur formation with gravity and magnetic fields in a stationary two arm spiral was made by Lee & Shu (2012) and Lee (2014). Renaud et al. (2014) suggested that the regularly spaced condensations inside spiral arms are from gravitational instabilities, and the spurs that trail the arms are from Kelvin-Helmholtz-type instabilities.

To investigate the role of gravitational collapse in galactic-scale filaments, we examined for this paper Spitzer Space Telescope InfraRed Array Camera (IRAC) images of nearby spiral galaxies from the Spitzer image archive (e.g., NGC 300, M74, M63, M83, M100, M101, NGC 6946, IC 342). All of these galaxies were found to contain bright infrared (IR) condensations, or “clumps,” somewhat regularly spaced along thin dust filaments that sometimes extend for several kpc. Because these structures could be a key to understanding how spiral waves trigger star formation, we chose one example, M100, and measured the clump properties from the archival images. Clumps in the nuclear ring of M100 were studied previously by Knapen et al. (1995). The clumps in the spiral arms observed here are found to have little correspondence with optical features, suggesting embedded or highly obscured star formation if they are powered internally. This latter result needs further study, perhaps with higher resolution IR observations, because Prescott et al. (2007) and Schinnerer et al. (2013) found relatively little embedded star formation in the galaxies they observed. Our previous observations (Elmegreen et al. 2014) found a few regions that were visible in the IRAC bands and invisible in the SDSS images.

The first IRAC observations showing clumpy spiral arm structure were for M81 in Willner et al. (2004). Calzetti et al. (2005) studied clumps in the main spiral arms of M51, combining $8\mu\text{m}$ with $24\mu\text{m}$ and other observations in ~ 500 pc apertures to determine star formation rates. Foyle et al. (2013) also observed regularly spaced spiral arm clumps at IRAC $8\mu\text{m}$ and with Spitzer and Herschel FIR in M83; they found $10^6 - 10^8 M_{\odot}$ gas masses on

scales of 200-300 pc with heating mostly by internal star formation. The structures reported in the present paper are similar to these morphologically, but generally smaller and more pervasive, with diameters of ~ 130 pc and spacings of ~ 410 pc.

2. Observations

2.1. Morphology

Figure 1 shows an IRAC image of M100 from the Spitzer website¹. The image is a composite of $3.6\mu\text{m}$, $4.5\mu\text{m}$, $5.8\mu\text{m}$, and $8\mu\text{m}$ images. The galaxy is composed of numerous clumpy filaments in dust emission, which make it different from the usual view in optical images. The right-hand side of Figure 1 shows the Very Large Telescope (VLT) Focal Reducer and Low-Dispersion Spectrograph (FORs) image of M100 in optical bands R, V, and B to the same scale². The thin filaments and semi-regular spacings of clumps in the IRAC image are barely perceptible in the optical. Some IR filaments are dust lanes in optical light without any evidence for the clumps, some are haphazard strings of HII regions or bright irregular star complexes, and some are completely indistinct.

To highlight this difference, Figure 2 shows enlargements of select regions from the Spitzer and VLT images, displayed on the same scale. Most of the IR clumps are regularly spaced and similar to each other along the filaments, but the optical features are irregular in both extinction and emission from $\text{H}\alpha$ and young stars.

Figure 3 shows the ratio of the $8\mu\text{m}$ to the Spitzer MIPS $24\mu\text{m}$ emission. This ratio has the effect of removing the local background to highlight small-scale NIR features, like an unsharp-mask image. It occurs because the MIPS image has an angular resolution of $7.1''$, the $8\mu\text{m}$ image has a resolution of $2.4''$ (Chambers et al. 2009), and most of the $8\mu\text{m}$ features have $24\mu\text{m}$ counterparts. The ratioed image brings out the clumps well, showing them as white dots aligned along nearly all of the larger-scale structures.

¹credit: NASA/JPL-Caltech; www.spitzer.caltech.edu/images/5208-sig12-007-The-Swirling-Arms-of-the-M100-Galaxy

²credit: ESO; <http://eso.org/public/images/potw1330a/>

2.2. Measurement of Clump Properties

The Spitzer image of M100 was examined for small bright clumps with central peaks and red colors. Several small white clumps were avoided as they were thought to be young regions that have partially broken through the dust. Stars are very blue in these images and were easily avoided.

The position and flux of each clump were first measured in four IRAC bands using the Image Reduction Analysis Facility (IRAF) task *phot* with a measurement aperture of 2 pixels radius and background subtraction from an annulus between 3 and 4 pixels away from the center. This background region was chosen because the clumps tend to be separated by 7 pixels (see below), and then the background lies between the clumps. The zero points for conversion of counts to magnitudes were taken from the IRAC Instrument handbook³. The positions and magnitudes for the clumps in the filaments are given in Table 1.

Another set of measurements was made for the clumps on the filaments. Here, the clump fluxes were determined with *phot* in a 1.5 pixel radius aperture with no background annulus, and a background for subtraction was determined from other *phot* 1.5 pixel apertures located midway between each pair of clumps. Thus, for this second set, the background for subtraction was taken to be the average of the fluxes from the two filament midpoints on either side of the clump; for clumps at the ends of the filaments, the background was taken to be the flux from the one adjacent filament midpoint. This second measurement using filament midpoints as backgrounds was designed to get the brightnesses of the clumps relative to the adjacent filaments, and also the color excesses of the clumps relative to the colors of the adjacent filaments. The clump magnitudes determined in this second way are listed in Table 2, including only those with measurable interclump fluxes.

Clumps were selected for measurement based on their compactness and brightness. For the first method discussed above, they are complete down to ~ 13.5 mag at $8\mu\text{m}$, ~ 15.5 mag at $5.6\mu\text{m}$, ~ 18 mag at $4.5\mu\text{m}$ and ~ 18 mag at $3.6\mu\text{m}$. We determined these limits by blocking each chosen clump with a black dot on Figure 3 as we measured it, using the clump position to the nearest half pixel, and then measuring fainter and fainter clumps until it was clear there were no remaining small clumps brighter than the limits. This does not count multiple or highly elliptical clumps or elongated bright regions that have larger total brightnesses, as we are interested only in compact clumps like those that dot the filaments. We also ran SExtractor to search for clumps on several types of images, including Figures 1 and 3, but the background varies too much from clump to clump to get any reasonable

³http://irsa.ipac.caltech.edu/data/SPITZER/docs/irac/irac_instrumenthandbook/

match to what we could find by eye.

In the end, we selected 422 clumps as representative of the whole galaxy. Of these, 147 are in 27 filaments, most of which have a spiral-like appearance or are in the main stellar density wave arms. Figure 4 identifies the 147 filament clumps using different symbols and colors for each filament. The 275 non-filament clumps are shown as black dots. There are many more clumps that are diffuse or faint that are ignored.

2.3. Separation Distribution

Figure 5 plots on the left the distribution function of the separation between adjacent clumps on each filament with 3 or more clumps. The units are in pixels on the Spitzer FITS images, which are $0.75''$ in size. A pixel corresponds to 59 pc at a distance of 16.2 Mpc from NED⁴. The peak in the distribution at 7 pixels corresponds to 410 pc. This separation distribution does not consider the inclination of the galaxy, which is 30° (Knapen et al. 2002); deprojection would increase the separations by at most 13% along the major axes, which is not significant.

The right-hand side of Figure 5 shows as a histogram the relative difference in the separations between three adjacent clumps, calculated as $2(S_{i,i-1} - S_{i+1,i})/(S_{i,i-1} + S_{i+1,i})$ for adjacent clump indices $i - 1$, i and $i + 1$ along a filament and separations S . The relative difference in separation is small and it shows two peaks, one within 0.2 of 0 and another around 0.66. The first peak corresponds to equal separations between clumps, i.e., a regularity in their position along the filament. The second peak corresponds to a gap in a regular spacing. That is, for a gap in the midst of a regular spacing of 1 unit, the distance between the first two clumps that straddle the gap is 2 units, and the distance between the next two clumps in the sequence is 1 unit. Thus the relative difference is $2 \times (2 - 1)/(2 + 1) = 0.66$. According to the right-hand side of Figure 5, 48 relative separations out of the total of 93 (52%) in the plot are regular or regular with a gap where there is one missing. This confirms the appearance by eye of the regularity of the clumpy filaments in Figures 1 to 3.

Also on the right of Figure 5, there are circles and horizontal error bars representing the mean and variance, which show the number of clumps on each filament (y -axis) versus the relative separations along these filaments (x -axis). Only filaments with more than 3 clumps are considered. The points show a more precise regularity, i.e., a smaller number on the

⁴<https://ned.ipac.caltech.edu/>

x -axis, for filaments that contain fewer clumps. Longer filaments with many clumps have a slightly more irregular spacing between the clumps. For clarity in plotting, the vertical dimension is offset from the integer number of clumps in the filament by a small random amount.

2.4. Magnitude Distribution

Figure 6 shows, in blue, the apparent magnitude distribution function at $8\mu\text{m}$ for all 422 clumps. This distribution is complete in the bright part beyond the peak (see above). Figure 6 also shows, in red, the magnitude distribution for clumps in all of the identified filaments, and in black, the clumps in the main spiral arm, which is to the west and south of the center (the corresponding symbols in Figure 4 are magenta squares, cyan squares and green crosses). The main spiral arm has brighter clumps than elsewhere, as evident also from the optical image. The luminosity scale at the top of this figure is from the conversion of flux density into luminosity, assuming a width for the IRAC4 filter equal to $2.88\mu\text{m}$, from the half-power points given in the IRAC instrument handbook, page 18. The distance modulus is 31.05.

The right-hand part of Figure 6 plots as a histogram the differences in $8\mu\text{m}$ magnitudes between adjacent clumps. The circles and horizontal lines are the means and variances of the magnitude differences for each filament with more than 2 clumps (as opposed to more than 3 clumps for the separation differences). The dispersion in the histogram for the differences is 0.46 mag., and the dispersion in the magnitudes themselves, from the left-hand panel, is 1.01 mag. The expected dispersion of a random sample of differences drawn from a Gaussian distribution like the magnitude distribution on the left is $\sqrt{2}$ times the dispersion of the Gaussian, which would be 1.42 mag in our case. The dispersion of the observed differences is only 0.32 times the expected dispersion of the differences if the adjacent clumps were drawn from a random sample. Thus the adjacent clumps are closer to each other in $8\mu\text{m}$ brightness than they would be in a random distribution, by a factor of 3.1. We get approximately the same result considering only clumps brighter than 13.5 mag at $8\mu\text{m}$ for the total magnitude dispersion (0.76 mag in that case) and considering only adjacent clumps where both are brighter than 13.5 mag at $8\mu\text{m}$ (0.42 mag dispersion for the mag differences), giving the ratio 2.5. These results, combined with the regularity shown in Figure 5, suggest that clump formation in galactic-scale filaments is a coherent process.

2.5. Color Distribution

Figure 7 shows color-magnitude and color-color diagrams of the clumps, where the colors and magnitudes were determined in the two ways mentioned above, once with background subtraction from an annulus that lies between the clumps on average (top panels), and again with the filament brightness used for the background subtraction (middle panels). The similarity of the $3.6\mu\text{m}$ and $4.5\mu\text{m}$ fluxes ($[3.6]-[4.5]$ is small) and the red colors at $5.8\mu\text{m}$ and $8\mu\text{m}$ indicate the presence of stars at the shorter wavelengths and warm dust and PAH emission at the longer wavelengths.

In the top panels the $[3.6] - [4.5]$ color averages 0.20 ± 0.03 mag with dispersion $\sigma = 0.33$ mag; the $[4.5] - [5.6]$ color averages 2.17 ± 0.03 mag with $\sigma = 0.40$ mag, and the $[5.8] - [8.0]$ color averages 1.75 ± 0.02 mag with $\sigma = 0.19$ mag. In the middle panels, the $[3.6] - [4.5]$ color averages 0.31 ± 0.02 mag with $\sigma = 0.27$ mag; the $[4.5] - [5.6]$ color averages 2.04 ± 0.05 mag with $\sigma = 0.50$ mag, and the $[5.8] - [8.0]$ color averages 1.71 ± 0.02 mag with $\sigma = 0.21$ mag.

These colors compare well with models of emission from star-forming regions. Dale et al. (2001) show model galaxy spectra with a jump equal to factor of ~ 5 from $4.5\mu\text{m}$ to $5.8\mu\text{m}$ in their figure 5, and that factor corresponds to a color of $[4.5] - [5.8] = 1.75$ mag. Gutermuth et al. (2009) consider PAH colors as a source of contamination for studies of protosars in star-forming regions; their figure 15 shows the PAH region in color-color space where $[4.5] - [5.8] \sim 1$ to 2 and $[3.6] - [4.5] \sim 0$ to 1 , as for our colors. Protostar envelopes are redder in $[3.6] - [4.5]$ than our clumps because of their hotter dust, and protostar disks are bluer in $[5.8] - [8.0]$ (Allen et al. 2004). The IRAC colors of the diffuse interstellar medium in the Milky Way are also close to our $[4.5] - [5.8]$ colors. Flagey et al. (2006) measure these colors outside regions of star formation and tabulate the ratios in their Table 1. Typically the ratio of $4.5\mu\text{m}$ to $5.8\mu\text{m}$ emission is $\sim 1/8$, which corresponds to a color of ~ 2.3 , similar to that in Figure 7. The ratio of $5.8\mu\text{m}$ to $8.0\mu\text{m}$ in Flagey et al. (2006) is smaller, ~ 0.3 , which corresponds to a color of 1.2 mag, whereas we measure $[5.8] - [8.0] \sim 1.5$ to 2 in the top panels of Figure 7. This difference implies that the $8\mu\text{m}$ emission is relatively larger in the M100 clumps than in local diffuse clouds. Without longer wavelength observations at comparable resolution (the clumps are a few arcseconds in size), we cannot make a more complete spectral energy distribution (SED) and determine the contributions from stars and dust, nor can we get the dust temperature and total dust luminosity.

The bottom panels in Figure 7 show the excess colors of the clumps compared to the filaments. There is a lot of scatter, but the clumps are slightly redder in $[3.6] - [4.5]$, by 0.044 ± 0.005 mag, than the adjacent filaments (with $\sigma = 0.06$), about the same in $[4.5] - [5.8]$ with an excess of only 0.042 ± 0.010 mag ($\sigma = 0.12$), and slightly bluer in $[5.8] - [8.0]$, with

an excess of -0.011 ± 0.004 mag ($\sigma = 0.05$). These excesses suggest the filaments show a little more underlying disk starlight than the clumps.

2.6. Equivalent Stellar Masses

The equivalent stellar masses that excite the clumps can be determined from the IRAC fluxes and the bolometric magnitude of a young stellar population. These stellar masses do not necessarily correspond to embedded stars because some of the heating can come from adjacent stars that are visible optically. Nevertheless, they provide a measure of the associated young stellar mass for each clump.

We first estimate the total IR luminosity for the clumps using the complete SEDs of galaxies tabulated by Xu et al. (2001). This tabulation gives flux density versus wavelength for 6 normal galaxies with $24\mu\text{m}$ luminosities in the range from $10^6 L_\odot$ to $10^{10.6} L_\odot$, and for 2 starburst galaxies with $24\mu\text{m}$ luminosities equal to $10^8 L_\odot$ and $10^{11} L_\odot$. The SEDs from Xu et al. (2001) were integrated over the total width of the four IRAC bands, which is from $3.18\mu\text{m}$ to $9.33\mu\text{m}$ (the lower half-power point for the $3.6\mu\text{m}$ band and the upper half-power point for the $8\mu\text{m}$ band, according to the IRAC instrument handbook), and they were also integrated over the full SED to give the total IR flux. The ratio of the total to the IRAC fluxes ranged from 22 for the lowest-mass normal galaxy to 12 for the highest mass normal galaxy, and it was equal to 9.6 and 7.1 for the two starburst galaxies, respectively. The high values for low-mass normal galaxies reflect the dominance of background radiation on the dust heating as there is little star formation in these systems. The values decrease with increasing prominence of star formation because the PAH emission and hot dust emission in the IRAC bands goes up relative to the cool dust emission at longer wavelengths. We consider our clump SEDs to be most like the starburst SEDs because they enclose or are adjacent to regions of active star formation, as indicated by the juxtaposition of the clumps to HII regions and OB associations in Figure 2. Thus we take a ratio of ~ 8 to convert the summed flux in all four IRAC bands to the total IR luminosity.

This ratio is consistent with the ratios of total IR luminosity to $24\mu\text{m}$, which is about 10, and $8\mu\text{m}$ to $24\mu\text{m}$ luminosity, which is about unity, for M51 where longer wavelengths were measured (Calzetti et al. 2005). It is similar also to that in Dale et al. (2005), who observe an approximately flat normalized flux density distribution, νf_ν versus the logarithm of the wavelength for galaxies in the SINGS survey, considering that the ratio of the log-wavelength interval for the whole spectrum to the log-wavelength interval for IRAC is about 5 (that would make the total IR flux ~ 5 times the summed IRAC flux).

To convert the total IR luminosity to the mass of associated young stars, we use the bolometric magnitude of a young stellar population given in Bruzual & Charlot (2003). This is -2.7944 for solar metallicity at less than 1 Myr age and -1.0321 at 10 Myr. Using 4.74 mag as the bolometric magnitude of the Sun, the bolometric luminosity per solar mass of young stars is $3.01 \times 10^{35} \times 10^{0.4 \times 2.7944}$ at 1 Myr age, and the inferred stellar mass is the inverse of this quantity multiplied by the total IR luminosity of the clump. All of the clump masses would be larger by the factor 5.1 for an age of 10 Myr.

A histogram of the equivalent stellar masses for all 422 clumps at 1 Myr assumed age is shown in Figure 8. The average value of the log of the mass, in solar masses, is 3.5 ± 0.2 . This is reasonable for common, but bright, star-forming regions in spiral galaxies. The sum of the masses of the clumps in the filaments is $8.9 \times 10^5 M_\odot$. If the typical clump age is 10 Myr, then the associated stellar mass increases to $4.5 \times 10^6 M_\odot$ for the filament clumps, based on the lower bolometric luminosity per unit stellar mass given above.

3. Origin of the IR Clumps

The equal spacings and similar magnitudes of the clumps on the filaments suggests that the condensations formed by a regular process such as a gravitational instability along the filament lengths. The separation should be the length of the fastest growing unstable mode. The appearance of multiple clumps on filaments, sometimes with a half-dozen or more clumps, also implies that all parts of the filament formed at about the same time. Then all of the clumps collapsed together before the filaments could be dispersed by shear and star-formation feedback.

Filament instabilities without a magnetic field were studied early on by Ostriker (1964) and Inutsuka & Miyama (1992), and with a magnetic field by Chandrasekhar & Fermi (1953), Stodólkiewicz (1963), Nagasawa (1987), Nakamura et al. (1993), Tomisaka (1995), Fiege & Pudritz (2000) and others. When the filament has the equilibrium mass per unit length, $\mu = 2\sigma^2/G$ for velocity dispersion σ , these authors found a dominant wavelength, or separation between condensations, that is about 3.9 times the effective filament diameter, D_{eff} , which is $D_{\text{eff}} = 2\mu(\pi\rho_c)^{-1/2}$ for central density ρ_c . The growth rate for this mode is $\omega = 0.34 \times (4\pi G\rho_c)^{1/2}$. A filament confined by high pressure has a longer dominant wavelength and a slower growth rate because the mass per unit length is less at the same central density. A magnetic filament with an aligned field has about the same dominant wavelength if it is not highly confined by pressure because the instability occurs in a direction where the field exerts little force. If it is confined by pressure, then the field slows the growth as the wavelength increases.

Figure 2 shows good agreement with these expectations for the self-gravitational collapse of filaments. The separations appear to be 3 to 5 times the filament diameters, as expected for near-critical line densities. Figure 9 shows this more quantitatively. It plots a histogram of the ratio of the separation between adjacent clumps to the average clump diameter. The diameters were determined from the number of pixels in rectangles surrounding the clumps using the IRAF routine *imstat*. We consider that the rectangles typically go to about 0.1 times the peak brightness and we assume the diameters go to 0.5 times the peak brightness. In this case the diameters used for Figure 9 are about 1.1 times the square roots of the ratios of the areas to π , measured in pixels like the separations. Figure 9 has a clear peak in the ratio of separation to diameter that is centered at around 3, and a tail toward a value of ~ 6 that could be from adjacent clumps with a gap between them (see Fig. 4). This is the ratio expected if the clumps formed by gravitational instabilities.

The average gas densities inside the filaments are low because their apparent sizes are large. For example, if the gas mass is ~ 100 times the average stellar mass in Figure 8, which would be $\sim 3 \times 10^5 M_{\odot}$ corresponding to a low star-formation efficiency, and their diameters are typically ~ 130 pc as measured from the surrounding box sizes discussed above, then the average gas density is ~ 2.1 atoms cm^{-3} . Taking this density to be ρ_c in the above equation, the corresponding collapse time is $t_{\text{coll}} = 2.9(4\pi G\rho_c)^{-1/2} \sim 46$ Myr. This density is too low and the resulting time is too long to have a simultaneous collapse of many clumps along each filament. The filaments probably last only 10 Myr up to a few times 10 Myr, considering the distortions and shear of spiral arms. Thus the average gas density inside the filaments is probably much higher than what we see at the resolution of IRAC.

Dense filaments like the infrared dark clouds in the Milky Way (IRDC; e.g. Rathborne et al. 2007; Peretto & Fuller 2009) could be at the cores of our IRAC filaments. IRDC are opaque clouds observed against the bright background of diffuse IR emission from the Galactic plane. There is a 160 to 430 pc long IRDC in the Scutum-Centaurus Arm (Goodman et al. 2014) that is a good candidate for a galactic scale filament like the longer ones observed here. Jackson et al. (2010) also suggested that a self-gravitational instability made regular condensations in the Milky Way filament named “Nessie,” although that is on a much smaller scale with a 4.5 pc clump separation and a total length of 80 pc.

The kiloparsec lengths of many IRAC filaments imply that dynamical processes sweep up interstellar gas on this scale. For the main spiral arms, this process is presumably the usual density wave shock, which can have a length of several kpc for most of the regions inside corotation and possibly outside corotation too. The main spiral arms in M100 are of this type, as evident from the similar positions of broad stellar arms seen at $2\mu\text{m}$ wavelength

by the 2MASS survey (Skrutskie et al. 2006)⁵. Other filaments could be from shear inside the stellar arms, making spurs (Section I). Figures 1 to 2 show more remote filaments too, with no apparent connection to the stellar arms seen in the 2MASS image. These remote filaments suggest there are large-scale gas motions independent of the main stellar spirals, possible from local instabilities or stellar feedback.

If the evolution timescale for the filaments is ~ 10 Myr, based on the expectation of shear rates and spiral wave motions, and the total mass of the measured clumps in the filaments is $4.5 \times 10^6 M_\odot$ for this age, from above, then the ratio of the mass to the age is $0.45 M_\odot \text{ yr}^{-1}$, which is lower than the total star formation rate in M100, $\sim 2.6 M_\odot \text{ yr}^{-1}$ (Kennicutt et al. 2011). For a 1 Myr timescale, the rate would be $0.89 M_\odot \text{ yr}^{-1}$, which is still small. These small rates suggest that filament clumps are not the only drivers of star formation in M100. This conclusion is consistent with the other evidence given in the introduction that spiral waves affect the total star formation rate by only small amounts. It is also consistent with the appearance of many other star forming regions outside of the filaments. Still, the appearance of highly regular clump structures in numerous long filaments suggest that spiral arms trigger gas collapse and at least some cloud formation by gravitational instabilities.

4. Conclusions

Dust filaments in M100 revealed by Spitzer IRAC images tend to have a regular spacing of similar-mass clumps along their lengths, suggestive of a formation process involving gravitational instabilities in gas that was accumulated by the relative motion of spiral density waves and the associated large-scale flows. The clump separation is typically 410 pc and the ratio of the separation to the clump diameter ranges from 2 to 4. Many filaments extend for several kpc. These regions appear to be galactic-scale analogs of local star-forming filaments and filamentary IRDCs, and they probably form and evolve in a similar way, making stars at the gravitating condensations. IRAC colors reflect their likely emission from PAHs and hot dust, as modelled for galactic star-forming regions. The effective stellar masses of the selected condensations average $3 \times 10^3 M_\odot$ for an age of 1 Myr, with a total effective mass in the range of $0.9 - 4.5 \times 10^6 M_\odot$ for the measured clumps in the filaments if we assume ages of 1 Myr and 10 Myr, respectively. The ratio of these filament clump masses to the assumed ages fall short of the star formation rate in M100 by factors of 3 to 6, which is consistent with the relatively small influence that spiral arms generally have on total star formation rates. The importance of the observation lies in the identification of one process by which

⁵<https://www.ipac.caltech.edu/2mass/gallery/m100atlas.jpg>

spiral waves interact dynamically with the interstellar medium to form new clouds.

Acknowledgments This research has made use of the NASA/IPAC Extragalactic Database (NED) which is operated by the Jet Propulsion Laboratory, California Institute of Technology, under contract with the National Aeronautics and Space Administration. This publication makes use of data products from the Two Micron All Sky Survey, which is a joint project of the University of Massachusetts and the Infrared Processing and Analysis Center/California Institute of Technology, funded by the National Aeronautics and Space Administration and the National Science Foundation. We are grateful to an anonymous referee for suggestions and to Eric Feigelson for comments on our statistical procedures.

REFERENCES

- Allen, L.E., Calvet, N., DAlessio, P. et al. ApJS, 154, 363
- André, Ph., Men'shchikov, A., Bontemps, S., et al. 2010, A&A, 518, L102
- W. Baade, 1963 in *The Evolution of Stars and Galaxies*, ed. C. Payne-Gaposchkin, Harvard Univ. Press: Cambridge, Chapter 16.
- Baba, J., Saitoh, T.R., & Wada, K. 2013, ApJ, 763, 46
- Baba, J., Morokuma-Matsui, K., & Saitoh, T.R. 2017, MNRAS, 464, 246
- Balbus, S. A. 1988, ApJ, 324, 60
- Benincasa, S.M., Tasker, E.J., Pudritz, R.E., Wadsley, J. 2013, ApJ, 776, 23
- Bettoni, D.; Buson, L. M., & Galletta, G. 2010, A&A, 519, 72
- Bonnell, I.A., Dobbs, C.L., Smith, R.J. 2013, MNRAS, 430, 1790
- Bruzual, G., & Charlot, S. 2003, MNRAS, 344, 1000
- Calzetti, D., Kennicutt, R.C., Jr., Bianchi, L., et al. 2005, ApJ, 633, 871
- Chakrabarti, S., Laughlin, G., & Shu, F. H. 2003, ApJ, 596, 220
- Chambers, E. T., Jackson, J. M., Rathborne, J.M., & Simon, R. 2009, ApJS, 181, 360
- Chandrasekhar, S. & Fermi, E. 1953, ApJ, 118, 116
- Colombo, D., Hughes, A., Schinnerer, E., et al. 2014, ApJ, 784, 3

- Comerón, S., Knapen, J. H., Beckman, J. E., et al. 2010, MNRAS, 402, 2462
- Cowie, L. L. 1981, ApJ, 245, 66
- Crocker, D. A., Baugus, P. D., & Buta, R. 1996, ApJS, 105, 353
- Dale, D.A., Helou, G., Contursi, A., Silbermann, N.A., & Kolhatkar, S, 2001, ApJ, 549, 215
- Dale, D.A., Bendo, G.J., Engelbracht, C.W., & Gordon, K.D., ApJ, 633, 857
- Dobbs, C. L., & Bonnell, I. A. 2006, MNRAS, 367, 873
- Dobbs, C.L. & Bonnell, I.A. 2008a, MNRAS, 385, 1893
- Dobbs, C. L., Glover, S. C. O., Clark, P. C., & Klessen, R. S. 2008b, MNRAS, 389, 1097
- Dobbs, C.L. 2008, MNRAS, 391, 844
- Dobbs, C. L., & Pringle, J. E. 2009b, MNRAS, 396, 1579
- Dobbs C. L., & Pringle J. E., 2010, MNRAS, 409, 396
- Dobbs, C. L., Burkert, A., Pringle, J. E. 2011, MNRAS, 417, 1318
- Dobbs, C.L., & Pringle, J.E. 2013, MNRAS, 432, 653
- Dobbs, C. L., Pringle, J. E., & Duarte-Cabral, A. 2015a, MNRAS, 446, 3608
- Dobbs, C.L. 2015b, MNRAS 447, 3390
- Donovan Meyer, J., Koda, J., Momose, R. et al. 2013, ApJ, 772, 107
- Duarte-Cabral, A., & Dobbs, C. L. 2016, MNRAS, 458, 3667
- Efremov, Yu. N. 2010, MNRAS, 405, 1531
- Egorov, O.V., Lozinskaya, T.A., Moiseev, A.V., & Shchekinov, Y.A. 2017, MNRAS, 464, 1833
- Elmegreen, B.G. 1979, ApJ, 231, 372
- Elmegreen, D.M. 1980, ApJ, 242, 528
- Elmegreen, B.G. 1994a, ApJ, 425, L73
- Elmegreen, B.G., & Elmegreen, D.M. 1983, MNRAS, 203, 31

- Elmegreen, B.G., & Elmegreen, D.M. 1986, *ApJ*, 311, 554
- Elmegreen, D.M., Elmegreen, B.G., Kaufman, M., et al. 2006, *ApJ*, 642, 158
- Elmegreen, D. M., Elmegreen, B. G., Erroz-Ferrer, S. et al. 2014, *ApJ* 780, 32
- Fiege, J.D. & Pudritz, R.E. 2000, *MNRAS*, 311, 105
- Flagey, N., Boulanger, F., Verstraete, L., et al. 2006, *A&A*, 453, 969
- Foyle, K., Natale, G., Wilson, C.D. et al. 2013, *MNRAS*, 432, 2182
- Goodman, A.A., Alves, J., Beaumont, C.N., et al. 2014, *ApJ*, 797, 53
- Gusev, A. S., & Efremov, Yu. N. 2013, *MNRAS*, 434, 313
- Gutermuth, R.A., Megeath, S.T., Myers, P.C., et al. 2009, *ApJS*, 184, 18
- Hirota, A., Kuno, N., Sato, N., et al. 2011, *ApJ*, 737, 40
- Inutsuka, S. & Miyama, S.M. 1992, *ApJ*, 388, 392
- Jackson, J.M., Finn, S.C., Chambers, E.T., Rathborne, J.M., & Simon, R. 2010, *ApJ*, 719, L185
- Kennicutt, R.C., Jr., Keel, W.C., Blaha, C.A. 1989, *AJ*, 97, 1022
- Kennicutt, R.C., Calzetti, D., Aniano, G., et al. 2011, *PASP*, 123, 1347
- Keto, E.R., Lattanzio, J.C., & Monaghan, J. J. 1991, *ApJ*, 383, 639
- Kim, W.-T., & Ostriker, E.C. 2001, *ApJ*, 559, 70
- Kim, W.-T., & Ostriker, E. C. 2002, *ApJ*, 570, 132
- Kim, T.-T., & Ostriker, E.C. 2006, *ApJ*, 646, 213
- Kim, W.-T., & Ostriker, E.C. 2007, *ApJ*, 660, 1232
- Kim, W.-T., Kim, Y., & Kim, J.-G. 2014, *ApJ*, 789, 68
- Kim, Y., Kim, W.-T., & Elmegreen, B. 2015, *ApJ*, 809, 33
- Knapen, J. H., Beckman, J. E., Shlosman, I., et al. 1995, *ApJ*, 443, L73
- Knapen, J. H., Pérez-Ramírez, D., & Laine, S. 2002, *MNRAS*, 337, 808

- Koda, J., Scoville, N., Sawada, T., et al. 2009, *ApJ*, 700, L132
- Kwan, J. & Valdes, F. 1983, *ApJ*, 271, 604
- La Vigne, M.A., Vogel, S.N., & Ostriker, E.C. 2006, *ApJ*, 650, 818
- Lee, W.-K. 2014, *ApJ*, 792, 122
- Lee, W.-K., & Shu, F. H. 2012, *ApJ*, 756, 45
- Lynds, B. T. 1970, in *IAU Symp. 38, The Spiral Structure of our Galaxy*, ed. W. Becker, & G. I. Contopoulos (Dordrecht: Reidel) 38
- Miettinen, O. 2018, *A&A*, 609, A123
- Mouschovias, T. Ch., Shu, F. H., & Woodward, P.R. 1974, *A&A*, 33, 73
- Myers, P.C. 2009, *ApJ*, 700, 1609
- Nagasawa, M. 1987, *Prog. Theor. Phys.*, 77, 635
- Nakamura, F., Hanawa, T., & Nakano, T. 1993, *PASJ*, 45, 551
- Ostriker, J. 1964, *ApJ*, 140, 1056
- Pastoriza, M.G. 1975, *Ap&SS*, 33, 173
- Peretto, N., & Fuller, G. A. 2009, *A&A*, 505, 405
- Prescott, M. K. M., Kennicutt, R. C., Jr., Bendo, J. W., et al. 2007, *ApJ*, 668, 182
- Puerari, I., Elmegreen, B.G., & Block, D.L. 2014, *AJ*, 148, 133
- Ragan S. E., Henning T., Tackenberg J., et al. 2014, *A&A*, 568, A73
- Rathborne, J. M., Simon, R., & Jackson, J. M. 2007, *ApJ*, 662, 1082
- Renaud, F., Bournaud, F., Emsellem, E., et al. 2013, *MNRAS*, 436, 1836
- Renaud, F., Bournaud, F., Emsellem, E., Elmegreen, B., & Teyssier, R. 2014, *ASPC*, 480, 247
- Roberts, W.W. 1969, *ApJ*, 158, 123
- Roberts, W.W., Jr., & Stewart, G.R. 1987, *ApJ*, 314, 10
- Sánchez-Monge, Á., Beltrán, M.T., Cesaroni, R., et al. 2014, *A&A*, 569, A11

- Sandage, A. 1961, *The Hubble Atlas of Galaxies*
- Schinnerer, E., Meidt, S.E., & Pety, J. et al. 2013, *ApJ*, 779, 42
- Schneider, S., & Elmegreen, B.G. 1979, *ApJS*, 41, 87
- Shabani, F., Grebel, E.K., & Pasquali, A. et al. 2018, *MNRAS*, tmp 1216
- Scoville, N. Z., Sanders, D. B., & Clemens, D. P. 1986, *ApJ*, 310, L77
- Shetty, R. & Ostriker E.C. 2006, *ApJ*, 647, 997
- Shu, F.H., Milione, V., Gebel, W., et al. 1972, *ApJ*, 173, 557
- Skrutskie, M.F., Cutri, R.M., Stiening, R. et al. 2006, *AJ*, 131, 1163
- Sormani, M.C., Sobacchi, E., Shore, S.N., Tress, R.G. & Klessen, R.S. 2017, *MNRAS*, 471, 2932
- Stodólkiewicz, J.S. 1963, *Acta. Astron.* 13, 30
- Tempel, E., Kipper, R., Saar, E., et al. 2014, *A&A*, 572, A8
- Tomisaka, K. 1987, *PASJ*, 39, 109
- Tomisaka, K. 1995, *ApJ*, 438, 226
- Tremblay, G.R., Gladders, M. D., Baum, S.A. et al. 2014, *ApJ*, 790, L26
- Väisänen, P., Barway, S., & Randriamanakoto, Z. 2014, *ApJ*, 797, L16
- van der Laan, T. P. R., Schinnerer, E., Emsellem, E., et al. 2013, *A&A*, 551A, 81
- Wada, K., & Koda, J. 2004, *MNRAS*, 349, 270
- Wang, Z., Fazio, G.G., Ashby, M. L. N., et al. 2004, *ApJS*, 154, 193
- Willner, S. P., Ashby, M. L. N., Barmby, P., et al. 2004 *ApJS*, 154, 222
- Xu, C., Lonsdale, C.J., Shupe, D.L., O’Linger, J., & Masci, F. 2001, *ApJ*, 562, 179
- Yuan, C., & Grosbol, P. 1981, *ApJ*, 243, 432

Table 1. Clumps in Filaments with Background Annulus Subtracted

RA	DEC	[3.6] mag	[4.5] mag	[5.8] mag	[8.0] mag
Filament 1,	blue <i>o</i>				
12:22:46.4110	15:48:37.915	17.86 ± 0.89	17.71 ± 1.03	15.48 ± 0.47	13.52 ± 0.26
12:22:46.4110	15:48:34.165	17.41 ± 0.72	17.18 ± 0.81	14.93 ± 0.36	13.16 ± 0.22
12:22:46.3851	15:48:28.540	17.58 ± 0.79	17.45 ± 0.92	15.35 ± 0.45	13.66 ± 0.31
12:22:46.4371	15:48:25.915	16.84 ± 0.57	16.43 ± 0.58	14.81 ± 0.36	13.08 ± 0.25
Filament 2,	green triangle				
12:22:47.9173	15:49:52.543	18.57 ± 1.23	18.35 ± 1.38	15.60 ± 0.49	13.97 ± 0.34
12:22:47.6055	15:49:48.418	16.57 ± 0.49	16.31 ± 0.54	14.16 ± 0.26	12.34 ± 0.16
12:22:47.4237	15:49:43.542	15.33 ± 0.28	14.90 ± 0.28	13.03 ± 0.16	11.27 ± 0.11
12:22:47.0600	15:49:31.542	15.47 ± 0.30	15.11 ± 0.31	13.10 ± 0.16	11.38 ± 0.11
12:22:46.9042	15:49:24.791	16.93 ± 0.59	16.61 ± 0.63	14.34 ± 0.29	12.64 ± 0.20
12:22:46.7483	15:49:22.166	17.29 ± 0.69	17.13 ± 0.80	14.67 ± 0.33	13.00 ± 0.22
12:22:46.7743	15:49:19.916	17.44 ± 0.75	17.06 ± 0.77	15.18 ± 0.43	13.33 ± 0.25
12:22:46.8003	15:49:16.166	17.51 ± 0.76	17.25 ± 0.83	15.44 ± 0.46	13.62 ± 0.29
12:22:46.3846	15:49:12.040	18.27 ± 1.07	17.74 ± 1.05	16.21 ± 0.64	14.39 ± 0.40
Filament 3,	red <i>o</i>				
12:22:47.4508	15:47:51.792	18.52 ± 1.20	18.38 ± 1.40	15.98 ± 0.58	14.14 ± 0.34
12:22:47.6327	15:47:48.418	18.06 ± 0.98	17.86 ± 1.11	16.06 ± 0.61	14.26 ± 0.41
12:22:47.7367	15:47:43.543	17.22 ± 0.66	16.95 ± 0.73	14.80 ± 0.34	13.03 ± 0.21
Filament 4,	cyan <i>x</i>				
12:22:49.5802	15:50:13.546	17.42 ± 0.73	17.43 ± 0.92	14.94 ± 0.37	13.19 ± 0.23
12:22:49.2165	15:50: 6.046	17.81 ± 0.87	17.44 ± 0.91	15.40 ± 0.48	13.60 ± 0.35
12:22:48.9826	15:50: 2.670	18.37 ± 1.14	18.11 ± 1.25	15.92 ± 0.60	14.19 ± 0.41
12:22:48.8787	15:49:58.920	16.56 ± 0.49	16.47 ± 0.58	14.03 ± 0.24	12.21 ± 0.15
12:22:48.7748	15:49:54.420	17.25 ± 0.67	17.01 ± 0.75	14.98 ± 0.38	13.21 ± 0.24
12:22:48.4630	15:49:52.169	19.17 ± 1.65	18.21 ± 1.31	16.16 ± 0.69	14.27 ± 0.44
12:22:48.2811	15:49:47.294	16.76 ± 0.54	16.58 ± 0.62	14.41 ± 0.29	12.68 ± 0.18
12:22:48.1252	15:49:45.419	17.05 ± 0.61	16.89 ± 0.71	14.64 ± 0.34	12.93 ± 0.24
12:22:47.8914	15:49:42.043	17.57 ± 0.78	17.33 ± 0.87	14.79 ± 0.34	13.26 ± 0.26
12:22:47.6057	15:49:30.793	18.19 ± 1.03	17.74 ± 1.04	15.38 ± 0.44	13.67 ± 0.29
12:22:47.1121	15:49:19.917	17.89 ± 0.90	17.74 ± 1.04	15.53 ± 0.49	14.00 ± 0.39
12:22:47.1641	15:49:17.667	18.19 ± 1.04	18.07 ± 1.22	15.71 ± 0.56	13.94 ± 0.38
12:22:47.1641	15:49:13.167	17.26 ± 0.68	17.16 ± 0.80	15.06 ± 0.40	13.24 ± 0.25
12:22:46.5925	15:49: 8.291	18.53 ± 1.25	18.39 ± 1.45	16.49 ± 0.78	14.69 ± 0.53
12:22:46.4887	15:49: 3.040	18.05 ± 0.98	17.92 ± 1.13	15.69 ± 0.55	14.03 ± 0.38
12:22:46.3588	15:49: 1.165	18.31 ± 1.10	18.13 ± 1.25	16.88 ± 0.99	15.33 ± 0.79
12:22:46.2289	15:48:58.165	19.87 ± 2.33	21.50 ± 6.36	17.29 ± 1.29	15.91 ± 1.38
Filament 5,	magenta triangle				
12:22:50.2044	15:48:48.797	17.42 ± 0.72	17.33 ± 0.86	15.13 ± 0.39	13.27 ± 0.23
12:22:50.0226	15:48:37.922	18.38 ± 1.12	18.27 ± 1.34	16.08 ± 0.61	14.38 ± 0.38
12:22:50.3345	15:48:25.922	18.99 ± 1.49	18.59 ± 1.55	16.17 ± 0.65	14.33 ± 0.37
Filament 6,	green +				
12:22:51.1132	15:51: 0.423	18.01 ± 0.95	18.15 ± 1.26	16.01 ± 0.65	14.00 ± 0.38
12:22:50.9572	15:51: 3.798	17.84 ± 0.89	17.60 ± 0.98	15.82 ± 0.56	13.64 ± 0.27
12:22:50.6713	15:51: 6.048	19.19 ± 1.68	19.05 ± 1.94	16.01 ± 0.59	14.54 ± 0.42

Table 1—Continued

RA	DEC	[3.6] mag	[4.5] mag	[5.8] mag	[8.0] mag
Filament 7,	magenta x				
12:22:52.1528	15:50:24.049	17.91 ± 0.91	17.33 ± 0.87	15.32 ± 0.43	13.50 ± 0.26
12:22:51.6591	15:50:24.424	17.10 ± 0.63	16.92 ± 0.72	14.56 ± 0.31	12.92 ± 0.21
12:22:51.2433	15:50:24.798	17.54 ± 0.77	16.86 ± 0.70	14.53 ± 0.31	12.58 ± 0.17
12:22:50.8275	15:50:25.923	18.39 ± 1.17	18.16 ± 1.27	15.69 ± 0.52	13.62 ± 0.32
12:22:50.4897	15:50:24.048	16.72 ± 0.53	16.51 ± 0.59	14.45 ± 0.29	12.67 ± 0.18
Filament 8,	magenta $+$				
12:22:51.6849	15:51: 9.424	17.20 ± 0.65	17.03 ± 0.75	14.89 ± 0.35	13.25 ± 0.23
12:22:51.4250	15:51:14.299	18.10 ± 0.99	17.81 ± 1.08	16.20 ± 0.67	14.19 ± 0.37
12:22:51.1131	15:51:14.298	18.31 ± 1.10	18.07 ± 1.22	15.91 ± 0.58	13.97 ± 0.32
Filament 9,	magenta square				
12:22:54.6476	15:49:33.050	14.94 ± 0.27	14.71 ± 0.28	12.97 ± 0.18	11.20 ± 0.15
12:22:54.0759	15:49:38.675	16.51 ± 0.48	16.16 ± 0.51	14.02 ± 0.24	12.28 ± 0.15
12:22:53.2444	15:49:39.800	16.87 ± 0.56	16.77 ± 0.67	14.66 ± 0.33	12.87 ± 0.20
12:22:52.5948	15:49:38.675	16.16 ± 0.41	15.60 ± 0.39	13.75 ± 0.23	12.06 ± 0.17
12:22:51.8672	15:49:35.299	16.62 ± 0.51	16.21 ± 0.52	13.99 ± 0.26	12.14 ± 0.19
12:22:51.6593	15:49:33.424	15.56 ± 0.32	15.12 ± 0.32	13.21 ± 0.20	11.35 ± 0.14
12:22:51.4255	15:49:30.424	15.01 ± 0.25	14.66 ± 0.26	12.63 ± 0.14	10.95 ± 0.10
12:22:51.1916	15:49:22.548	16.31 ± 0.44	16.12 ± 0.50	14.03 ± 0.25	12.20 ± 0.15
Filament 10,	cyan square				
12:22:50.8020	15:48:57.798	16.11 ± 0.40	15.98 ± 0.47	13.78 ± 0.22	12.02 ± 0.15
12:22:51.5556	15:48:49.549	16.88 ± 0.57	16.64 ± 0.63	14.56 ± 0.31	12.85 ± 0.20
12:22:51.8674	15:48:44.299	15.86 ± 0.35	15.49 ± 0.37	13.48 ± 0.19	11.78 ± 0.12
12:22:52.5430	15:48:44.300	18.11 ± 0.99	17.79 ± 1.07	15.49 ± 0.47	13.95 ± 0.32
12:22:52.7768	15:48:39.425	18.28 ± 1.09	18.02 ± 1.19	15.89 ± 0.57	13.84 ± 0.31
12:22:52.9327	15:48:37.550	18.32 ± 1.11	17.81 ± 1.09	16.12 ± 0.65	14.35 ± 0.46
12:22:53.2186	15:48:32.300	17.08 ± 0.62	17.00 ± 0.74	14.88 ± 0.36	13.19 ± 0.24
12:22:53.1926	15:48:29.675	17.81 ± 0.87	17.64 ± 1.01	15.02 ± 0.39	13.27 ± 0.26
12:22:54.1280	15:48:28.550	17.78 ± 0.88	17.85 ± 1.12	15.48 ± 0.47	13.48 ± 0.27
12:22:54.1539	15:48:24.050	17.35 ± 0.71	16.76 ± 0.66	14.75 ± 0.36	12.86 ± 0.21
12:22:54.2319	15:48:21.050	17.12 ± 0.63	16.78 ± 0.67	15.05 ± 0.44	13.76 ± 0.42
Filament 11,	red $+$				
12:22:54.0499	15:50:16.175	19.15 ± 1.66	18.27 ± 1.34	16.62 ± 0.88	15.28 ± 0.72
12:22:53.6601	15:50:18.800	18.41 ± 1.16	18.57 ± 1.56	15.78 ± 0.54	13.98 ± 0.33
12:22:53.3482	15:50:22.175	18.20 ± 1.04	17.85 ± 1.10	15.86 ± 0.56	14.95 ± 0.52
12:22:52.9584	15:50:24.050	17.57 ± 0.78	17.44 ± 0.91	15.16 ± 0.40	13.32 ± 0.25
12:22:52.7246	15:50:21.800	18.20 ± 1.04	18.01 ± 1.18	15.79 ± 0.54	13.78 ± 0.30
Filament 12,	green square				
12:22:55.4791	15:49:54.050	17.20 ± 0.65	17.08 ± 0.77	15.08 ± 0.38	13.28 ± 0.23
12:22:54.6736	15:49:58.925	17.72 ± 0.84	17.42 ± 0.90	15.62 ± 0.49	13.64 ± 0.27
12:22:54.3877	15:50: 1.550	18.04 ± 0.98	17.62 ± 0.99	15.35 ± 0.44	13.46 ± 0.25
12:22:54.1019	15:50: 4.550	17.16 ± 0.66	16.99 ± 0.75	15.00 ± 0.39	13.09 ± 0.24
12:22:53.9200	15:50: 2.300	17.70 ± 0.83	17.64 ± 1.01	15.40 ± 0.52	13.47 ± 0.34
12:22:53.6341	15:50: 0.425	17.73 ± 0.85	17.41 ± 0.91	15.38 ± 0.49	13.62 ± 0.35
12:22:53.1144	15:50: 3.800	17.47 ± 0.74	17.44 ± 0.91	16.02 ± 0.61	14.35 ± 0.41

Table 1—Continued

RA	DEC	[3.6] mag	[4.5] mag	[5.8] mag	[8.0] mag
12:22:52.7506	15:50: 5.300	18.57 ± 1.32	18.32 ± 1.39	15.69 ± 0.51	13.78 ± 0.29
12:22:52.4388	15:50: 2.300	18.25 ± 1.07	18.33 ± 1.38	15.69 ± 0.50	13.70 ± 0.28
12:22:51.7371	15:50: 6.049	17.59 ± 0.79	17.04 ± 0.76	15.39 ± 0.45	13.67 ± 0.29
Filament 13,	green <i>o</i>				
12:22:54.6735	15:51:23.300	18.62 ± 1.26	18.29 ± 1.34	15.78 ± 0.53	14.01 ± 0.32
12:22:54.3617	15:51:25.925	18.87 ± 1.42	18.43 ± 1.43	16.11 ± 0.62	14.54 ± 0.42
12:22:54.0758	15:51:27.050	19.93 ± 2.30	19.72 ± 2.60	17.03 ± 0.95	14.98 ± 0.51
12:22:53.6340	15:51:30.425	18.35 ± 1.12	18.17 ± 1.28	15.75 ± 0.53	14.09 ± 0.34
Filament 14,	green diamond				
12:22:55.9730	15:51: 2.675	16.48 ± 0.47	16.11 ± 0.49	14.24 ± 0.27	12.62 ± 0.19
12:22:55.8170	15:51: 7.550	17.60 ± 0.79	17.60 ± 0.98	15.26 ± 0.42	13.50 ± 0.26
12:22:55.5572	15:51:13.550	16.32 ± 0.44	16.07 ± 0.48	14.07 ± 0.24	12.14 ± 0.14
Filament 15,	green <i>x</i>				
12:22:57.7135	15:48: 6.424	15.17 ± 0.26	14.89 ± 0.28	12.76 ± 0.15	11.05 ± 0.11
12:22:57.1419	15:48: 6.800	15.33 ± 0.29	14.94 ± 0.30	12.85 ± 0.16	11.14 ± 0.12
12:22:56.6222	15:48: 7.925	15.91 ± 0.37	15.75 ± 0.43	13.84 ± 0.29	12.14 ± 0.25
12:22:56.2325	15:48:10.175	15.51 ± 0.30	15.21 ± 0.33	13.06 ± 0.16	11.34 ± 0.12
12:22:55.8688	15:48:11.675	15.68 ± 0.33	15.33 ± 0.35	13.20 ± 0.18	11.49 ± 0.13
12:22:55.3751	15:48:15.050	16.03 ± 0.38	15.79 ± 0.43	13.65 ± 0.20	11.87 ± 0.13
12:22:54.7515	15:48:16.925	15.07 ± 0.25	14.80 ± 0.27	12.73 ± 0.14	11.06 ± 0.11
Filament 16,	blue square				
12:22:56.7783	15:49: 4.550	18.19 ± 1.03	18.21 ± 1.29	15.51 ± 0.47	13.57 ± 0.26
12:22:57.3239	15:49: 4.550	17.06 ± 0.61	17.10 ± 0.78	15.52 ± 0.50	13.87 ± 0.39
12:22:57.5578	15:49: 6.049	17.29 ± 0.69	17.05 ± 0.76	15.21 ± 0.41	13.68 ± 0.31
12:22:57.8956	15:49: 9.049	17.80 ± 0.87	17.82 ± 1.10	15.37 ± 0.45	13.52 ± 0.29
Filament 17,	red square				
12:22:58.0775	15:49:19.549	19.10 ± 1.62	18.84 ± 1.74	16.61 ± 0.77	14.59 ± 0.42
12:22:57.8437	15:49:25.924	18.09 ± 1.00	17.77 ± 1.06	15.47 ± 0.46	13.88 ± 0.32
12:22:57.6618	15:49:25.174	18.80 ± 1.40	18.02 ± 1.20	15.38 ± 0.44	13.56 ± 0.27
12:22:57.4020	15:49:31.175	17.74 ± 0.84	17.70 ± 1.03	15.33 ± 0.44	13.48 ± 0.26
Filament 18,	red diamond				
12:22:58.3898	15:50:57.799	17.38 ± 0.71	17.08 ± 0.77	14.83 ± 0.34	13.05 ± 0.21
12:22:57.8441	15:51: 4.924	18.41 ± 1.14	18.01 ± 1.18	15.79 ± 0.53	13.95 ± 0.31
12:22:57.5323	15:51: 7.924	18.52 ± 1.20	18.12 ± 1.24	16.58 ± 0.78	14.97 ± 0.53
12:22:57.2724	15:51: 9.800	19.34 ± 1.75	19.23 ± 2.07	17.05 ± 0.96	15.13 ± 0.54
Filament 19,	cyan <i>o</i>				
12:22:59.1169	15:49:19.923	18.08 ± 0.99	18.02 ± 1.19	15.69 ± 0.52	13.75 ± 0.31
12:22:59.0390	15:49:28.173	17.89 ± 0.91	17.72 ± 1.04	15.33 ± 0.43	13.55 ± 0.26
12:22:58.7012	15:49:30.423	16.89 ± 0.57	16.32 ± 0.55	14.65 ± 0.35	13.12 ± 0.32
12:22:58.3634	15:49:35.299	17.18 ± 0.65	17.13 ± 0.79	15.21 ± 0.41	13.62 ± 0.30
12:22:58.1036	15:49:40.174	17.50 ± 0.75	17.10 ± 0.78	15.18 ± 0.40	13.42 ± 0.24
12:22:57.8698	15:49:42.424	18.81 ± 1.38	21.21 ± 6.01	16.78 ± 0.85	14.68 ± 0.45
12:22:57.5320	15:49:49.174	18.20 ± 1.06	17.80 ± 1.08	15.76 ± 0.54	13.80 ± 0.31
12:22:57.3761	15:49:51.050	18.37 ± 1.16	17.81 ± 1.10	15.78 ± 0.53	13.74 ± 0.28
Filament 20,	blue +				

Table 1—Continued

RA	DEC	[3.6] mag	[4.5] mag	[5.8] mag	[8.0] mag
12:22:59.1427	15:48:39.798	18.39 ± 1.15	18.04 ± 1.21	15.54 ± 0.47	13.86 ± 0.32
12:22:58.9348	15:48:39.798	18.33 ± 1.13	17.98 ± 1.19	16.47 ± 0.87	14.69 ± 0.68
12:22:58.5970	15:48:40.923	17.40 ± 0.73	17.24 ± 0.84	15.54 ± 0.50	14.25 ± 0.49
12:22:58.3372	15:48:41.299	17.73 ± 0.87	17.99 ± 1.24	15.21 ± 0.42	13.32 ± 0.24
12:22:58.1034	15:48:45.049	17.65 ± 0.81	17.33 ± 0.87	15.29 ± 0.44	13.56 ± 0.31
Filament 21, magenta <i>o</i>					
12:22:59.5585	15:48:54.797	15.82 ± 0.35	15.59 ± 0.39	13.28 ± 0.17	11.56 ± 0.11
12:22:59.2987	15:48:54.798	16.66 ± 0.57	16.43 ± 0.62	14.36 ± 0.40	12.60 ± 0.35
12:22:59.0128	15:48:54.048	16.91 ± 0.68	17.02 ± 0.90	14.60 ± 0.52	12.66 ± 0.38
12:22:58.7790	15:48:55.923	16.38 ± 0.47	16.08 ± 0.50	13.62 ± 0.22	12.00 ± 0.19
12:22:58.5971	15:48:56.673	15.91 ± 0.37	15.45 ± 0.37	13.62 ± 0.22	11.95 ± 0.17
12:22:58.3633	15:48:57.424	16.76 ± 0.54	16.50 ± 0.59	14.05 ± 0.24	12.30 ± 0.17
Filament 22, blue diamond					
12:23: 0.9365	15:50:45.045	17.76 ± 0.85	17.66 ± 1.00	15.36 ± 0.44	13.73 ± 0.28
12:23: 0.8066	15:50:49.545	17.93 ± 0.92	17.70 ± 1.02	16.00 ± 0.60	14.07 ± 0.33
12:23: 0.6507	15:50:52.546	18.48 ± 1.18	18.43 ± 1.44	15.79 ± 0.53	14.16 ± 0.35
Filament 23, red <i>x</i>					
12:23: 1.3263	15:50:40.169	16.89 ± 0.57	16.70 ± 0.65	14.38 ± 0.28	12.69 ± 0.18
12:23: 1.3783	15:50:46.544	17.50 ± 0.75	17.28 ± 0.84	15.11 ± 0.41	13.38 ± 0.27
12:23: 1.5083	15:50:49.169	17.05 ± 0.61	16.88 ± 0.71	14.78 ± 0.34	12.92 ± 0.19
Filament 24, red triangle					
12:23: 1.4819	15:50: 0.419	18.14 ± 1.01	18.23 ± 1.31	15.84 ± 0.55	14.20 ± 0.35
12:23: 1.3520	15:50: 8.294	18.08 ± 0.98	17.89 ± 1.11	15.80 ± 0.53	14.08 ± 0.34
12:23: 1.4821	15:50:21.044	18.47 ± 1.17	18.27 ± 1.33	15.96 ± 0.58	14.12 ± 0.36
Filament 25, blue <i>x</i>					
12:23: 2.4698	15:50:42.792	18.19 ± 1.03	18.41 ± 1.42	15.92 ± 0.58	14.10 ± 0.35
12:23: 2.5998	15:50:52.917	17.49 ± 0.75	17.37 ± 0.88	15.42 ± 0.45	13.64 ± 0.28
12:23: 2.5999	15:50:58.542	19.00 ± 1.50	19.01 ± 1.87	16.49 ± 0.76	15.28 ± 0.62
12:23: 2.4960	15:51: 3.792	19.05 ± 1.53	19.14 ± 1.99	16.53 ± 0.76	14.95 ± 0.51
12:23: 2.4181	15:51: 8.667	17.86 ± 0.89	17.94 ± 1.14	15.91 ± 0.56	13.92 ± 0.31
Filament 26, blue triangle					
12:23: 2.6245	15:48:48.417	17.88 ± 0.89	17.75 ± 1.05	15.40 ± 0.44	13.93 ± 0.32
12:23: 2.8324	15:48:50.666	18.82 ± 1.40	18.61 ± 1.57	16.01 ± 0.59	14.29 ± 0.40
12:23: 3.2222	15:48:54.790	18.11 ± 1.00	18.16 ± 1.27	15.98 ± 0.59	14.57 ± 0.41
Filament 27, cyan +					
12:23: 3.7676	15:48:36.039	18.20 ± 1.04	18.51 ± 1.50	16.90 ± 0.90	14.69 ± 0.48
12:23: 4.0795	15:48:45.413	17.54 ± 0.77	17.49 ± 0.93	16.10 ± 0.62	15.01 ± 0.55
12:23: 4.3654	15:48:51.038	17.92 ± 0.91	17.48 ± 0.93	15.69 ± 0.51	13.88 ± 0.31
12:23: 4.5734	15:48:58.162	19.06 ± 1.54	18.47 ± 1.46	16.28 ± 0.66	14.64 ± 0.43

Table 2. Clumps in Filaments with Interclump Subtracted

RA	DEC	[3.6] mag	[4.5] mag	[5.8] mag	[8.0] mag
Filament 1,	blue <i>o</i>				
12:22:46.4110	15:48:34.165	18.64 ± 0.85	18.28 ± 1.01	15.95 ± 0.49	14.19 ± 0.30
12:22:46.3851	15:48:28.540	19.70 ± 0.86	19.68 ± 1.04	17.71 ± 0.53	15.80 ± 0.33
12:22:46.4371	15:48:25.915	18.97 ± 0.74	18.25 ± 0.83	16.69 ± 0.44	15.08 ± 0.28
Filament 2,	green triangle				
12:22:47.6055	15:49:48.418	17.37 ± 0.62	17.06 ± 0.71	14.92 ± 0.34	13.10 ± 0.20
12:22:47.4237	15:49:43.542	15.69 ± 0.53	15.20 ± 0.60	13.24 ± 0.29	11.55 ± 0.18
12:22:47.0600	15:49:31.542	15.75 ± 0.57	15.36 ± 0.65	13.28 ± 0.31	11.57 ± 0.18
12:22:46.9042	15:49:24.791	17.89 ± 0.68	17.49 ± 0.77	15.59 ± 0.37	13.89 ± 0.22
12:22:46.7483	15:49:22.166	19.31 ± 0.75	18.94 ± 0.85	17.00 ± 0.41	15.46 ± 0.26
12:22:46.7743	15:49:19.916	19.57 ± 0.79	18.80 ± 0.89	17.41 ± 0.47	15.39 ± 0.29
12:22:46.8003	15:49:16.166	18.37 ± 0.83	18.17 ± 1.00	16.05 ± 0.52	14.14 ± 0.32
12:22:46.3846	15:49:12.040	18.21 ± 0.89	17.82 ± 1.07	15.84 ± 0.57	14.02 ± 0.36
Filament 3,	red <i>o</i>				
12:22:47.4508	15:47:51.792	19.80 ± 1.18	19.58 ± 1.45	17.10 ± 0.71	16.03 ± 0.45
12:22:47.6327	15:47:48.418	19.01 ± 1.06	18.64 ± 1.26	17.76 ± 0.70	15.85 ± 0.41
12:22:47.7367	15:47:43.543	17.72 ± 0.89	17.41 ± 1.04	15.27 ± 0.50	13.49 ± 0.30
Filament 4,	cyan <i>x</i>				
12:22:49.5802	15:50:13.546	18.19 ± 0.67	18.03 ± 0.82	15.68 ± 0.44	14.07 ± 0.27
12:22:49.2165	15:50: 6.046	18.63 ± 0.69	18.47 ± 0.85	16.20 ± 0.46	14.43 ± 0.28
12:22:48.8787	15:49:58.920	17.28 ± 0.58	17.06 ± 0.69	14.83 ± 0.34	13.02 ± 0.21
12:22:48.7748	15:49:54.420	18.32 ± 0.68	18.05 ± 0.81	16.70 ± 0.45	14.95 ± 0.28
12:22:48.4630	15:49:52.169	22.54 ± 0.90	21.13 ± 1.02	18.38 ± 0.55	16.36 ± 0.34
12:22:48.2811	15:49:47.294	17.81 ± 0.63	17.48 ± 0.74	15.61 ± 0.39	13.94 ± 0.25
12:22:48.1252	15:49:45.419	20.35 ± 0.73	20.49 ± 0.88	16.87 ± 0.41	14.81 ± 0.25
12:22:47.8914	15:49:42.043	18.47 ± 0.76	18.21 ± 0.90	15.65 ± 0.46	13.94 ± 0.29
12:22:47.6057	15:49:30.793	19.00 ± 0.87	18.60 ± 1.02	16.20 ± 0.54	14.44 ± 0.33
12:22:47.1121	15:49:19.917	19.65 ± 0.89	19.15 ± 1.04	16.77 ± 0.51	14.97 ± 0.32
12:22:47.1641	15:49:17.667	20.57 ± 0.94	19.65 ± 1.08	19.49 ± 0.59	16.37 ± 0.34
12:22:47.1641	15:49:13.167	18.05 ± 0.85	17.79 ± 1.03	15.52 ± 0.51	13.76 ± 0.31
12:22:46.5925	15:49: 8.291	18.86 ± 0.98	18.39 ± 1.18	16.76 ± 0.65	14.85 ± 0.39
12:22:46.4887	15:49: 3.040	19.53 ± 0.96	19.27 ± 1.19	17.16 ± 0.61	15.35 ± 0.37
12:22:46.3588	15:49: 1.165	21.17 ± 1.05	20.09 ± 1.22	18.32 ± 0.63	16.19 ± 0.38
Filament 5,	magenta triangle				
12:22:50.2044	15:48:48.797	17.90 ± 0.86	17.71 ± 1.05	15.58 ± 0.56	13.87 ± 0.35
12:22:50.0226	15:48:37.922	19.15 ± 1.04	18.66 ± 1.26	16.32 ± 0.66	14.61 ± 0.42
12:22:50.3345	15:48:25.922	20.07 ± 1.21	19.17 ± 1.43	16.81 ± 0.76	15.05 ± 0.49
Filament 6,	green +				
12:22:50.9572	15:51: 3.798	18.81 ± 0.94	18.68 ± 1.13	16.77 ± 0.60	14.67 ± 0.36
Filament 7,	magenta <i>x</i>				
12:22:52.1528	15:50:24.049	18.21 ± 0.70	17.77 ± 0.83	16.38 ± 0.50	15.43 ± 0.32
12:22:51.6591	15:50:24.424	17.71 ± 0.65	17.55 ± 0.79	15.34 ± 0.42	13.81 ± 0.26
12:22:51.2433	15:50:24.798	17.99 ± 0.64	17.57 ± 0.76	15.48 ± 0.40	13.70 ± 0.24
12:22:50.4897	15:50:24.048	17.03 ± 0.56	16.82 ± 0.66	14.77 ± 0.34	13.02 ± 0.20
Filament 8,	magenta +				

Table 2—Continued

RA	DEC	[3.6] mag	[4.5] mag	[5.8] mag	[8.0] mag
12:22:51.6849	15:51: 9.424	17.66 ± 0.94	17.48 ± 1.10	15.63 ± 0.53	13.90 ± 0.33
12:22:51.4250	15:51:14.299	18.60 ± 1.05	18.37 ± 1.24	16.92 ± 0.63	15.00 ± 0.38
12:22:51.1131	15:51:14.298	18.99 ± 1.09	18.74 ± 1.31	16.96 ± 0.66	15.22 ± 0.40
Filament 9,	magenta square				
12:22:54.6476	15:49:33.050	14.81 ± 0.32	14.56 ± 0.38	12.72 ± 0.23	11.02 ± 0.14
12:22:54.0759	15:49:38.675	17.18 ± 0.47	16.70 ± 0.55	14.51 ± 0.32	12.81 ± 0.20
12:22:53.2444	15:49:39.800	17.70 ± 0.55	17.52 ± 0.67	15.12 ± 0.37	13.44 ± 0.23
12:22:52.5948	15:49:38.675	16.52 ± 0.49	15.98 ± 0.56	13.99 ± 0.31	12.31 ± 0.19
12:22:51.8672	15:49:35.299	18.62 ± 0.53	18.69 ± 0.63	15.39 ± 0.31	13.48 ± 0.18
12:22:51.6593	15:49:33.424	17.02 ± 0.40	16.57 ± 0.44	14.98 ± 0.23	12.87 ± 0.14
12:22:51.4255	15:49:30.424	15.63 ± 0.36	15.29 ± 0.41	13.29 ± 0.20	11.61 ± 0.12
12:22:51.1916	15:49:22.548	18.40 ± 0.51	17.67 ± 0.60	16.73 ± 0.34	15.31 ± 0.21
Filament 10,	cyan square				
12:22:50.8020	15:48:57.798	16.88 ± 0.55	16.66 ± 0.65	14.24 ± 0.32	12.51 ± 0.20
12:22:51.5556	15:48:49.549	17.46 ± 0.58	17.49 ± 0.71	15.55 ± 0.37	14.11 ± 0.23
12:22:51.8674	15:48:44.299	16.13 ± 0.51	15.80 ± 0.61	13.77 ± 0.32	12.08 ± 0.19
12:22:52.5430	15:48:44.300	19.46 ± 0.74	19.03 ± 0.90	16.76 ± 0.50	15.32 ± 0.32
12:22:52.7768	15:48:39.425	20.14 ± 0.76	19.56 ± 0.92	17.57 ± 0.53	15.48 ± 0.32
12:22:53.2186	15:48:32.300	18.18 ± 0.65	17.98 ± 0.78	15.95 ± 0.41	14.26 ± 0.26
12:22:54.1280	15:48:28.550	19.72 ± 0.74	19.41 ± 0.91	18.60 ± 0.54	16.42 ± 0.33
12:22:54.1539	15:48:24.050	18.84 ± 0.65	17.92 ± 0.75	16.09 ± 0.39	14.24 ± 0.24
12:22:54.2319	15:48:21.050	17.95 ± 0.59	17.79 ± 0.70	16.74 ± 0.38	15.04 ± 0.24
Filament 11,	red +				
12:22:54.0499	15:50:16.175	22.55 ± 0.90	19.37 ± 0.95	17.26 ± 0.56	16.06 ± 0.37
12:22:53.6601	15:50:18.800	20.01 ± 0.78	19.49 ± 0.94	16.63 ± 0.53	14.67 ± 0.32
12:22:53.3482	15:50:22.175	18.82 ± 0.72	18.60 ± 0.88	16.96 ± 0.53	15.32 ± 0.34
12:22:52.9584	15:50:24.050	18.06 ± 0.67	17.82 ± 0.81	15.60 ± 0.44	13.84 ± 0.27
12:22:52.7246	15:50:21.800	23.92 ± 0.90	20.77 ± 0.97	20.40 ± 0.59	16.51 ± 0.32
Filament 12,	green square				
12:22:55.4791	15:49:54.050	17.29 ± 0.60	17.13 ± 0.74	15.04 ± 0.45	13.33 ± 0.29
12:22:54.6736	15:49:58.925	18.32 ± 0.65	18.05 ± 0.80	15.81 ± 0.48	14.04 ± 0.31
12:22:54.3877	15:50: 1.550	19.13 ± 0.68	18.74 ± 0.82	16.26 ± 0.48	14.52 ± 0.30
12:22:54.1019	15:50: 4.550	18.92 ± 0.65	18.58 ± 0.78	16.50 ± 0.44	14.54 ± 0.27
12:22:53.6341	15:50: 0.425	19.37 ± 0.69	18.97 ± 0.83	16.25 ± 0.48	14.73 ± 0.31
12:22:53.1144	15:50: 3.800	19.02 ± 0.68	19.06 ± 0.84	16.96 ± 0.53	15.29 ± 0.34
12:22:52.4388	15:50: 2.300	19.25 ± 0.72	19.53 ± 0.93	16.17 ± 0.53	14.28 ± 0.34
12:22:51.7371	15:50: 6.049	19.02 ± 0.70	18.07 ± 0.81	15.79 ± 0.50	14.00 ± 0.33
Filament 13,	green <i>o</i>				
12:22:54.3617	15:51:25.925	19.93 ± 1.26	19.84 ± 1.54	17.32 ± 0.73	16.23 ± 0.47
12:22:54.0758	15:51:27.050	20.61 ± 1.38	20.31 ± 1.66	17.73 ± 0.80	16.18 ± 0.49
12:22:53.6340	15:51:30.425	18.60 ± 1.18	18.43 ± 1.43	16.09 ± 0.69	14.54 ± 0.43
Filament 14,	green diamond				
12:22:55.9730	15:51: 2.675	17.35 ± 0.72	16.93 ± 0.83	15.19 ± 0.41	13.47 ± 0.25
Filament 15,	green <i>x</i>				
12:22:57.7135	15:48: 6.424	15.54 ± 0.39	15.35 ± 0.45	13.29 ± 0.21	11.69 ± 0.13

Table 2—Continued

RA	DEC	[3.6] mag	[4.5] mag	[5.8] mag	[8.0] mag
12:22:57.1419	15:48: 6.800	15.77 ± 0.42	15.35 ± 0.48	13.28 ± 0.22	11.63 ± 0.13
12:22:56.6222	15:48: 7.925	16.64 ± 0.49	16.38 ± 0.56	14.72 ± 0.27	13.18 ± 0.17
12:22:56.2325	15:48:10.175	16.18 ± 0.43	15.83 ± 0.48	13.76 ± 0.22	12.06 ± 0.14
12:22:55.8688	15:48:11.675	16.58 ± 0.44	16.11 ± 0.50	13.70 ± 0.23	11.98 ± 0.14
12:22:55.3751	15:48:15.050	16.83 ± 0.50	16.59 ± 0.59	14.38 ± 0.29	12.72 ± 0.18
12:22:54.7515	15:48:16.925	15.19 ± 0.44	14.92 ± 0.51	12.83 ± 0.24	11.15 ± 0.14
Filament 16,	blue square				
12:22:56.7783	15:49: 4.550	18.66 ± 0.60	18.79 ± 0.75	16.84 ± 0.47	15.46 ± 0.30
12:22:57.3239	15:49: 4.550	17.79 ± 0.55	17.81 ± 0.68	16.23 ± 0.42	14.88 ± 0.27
12:22:57.5578	15:49: 6.049	18.09 ± 0.56	17.80 ± 0.67	16.14 ± 0.41	14.65 ± 0.26
12:22:57.8956	15:49: 9.049	19.53 ± 0.61	18.87 ± 0.74	17.23 ± 0.46	15.21 ± 0.28
Filament 17,	red square				
12:22:58.0775	15:49:19.549	18.82 ± 0.67	18.36 ± 0.82	16.82 ± 0.55	15.15 ± 0.34
12:22:57.8437	15:49:25.924	19.18 ± 0.67	18.92 ± 0.82	16.16 ± 0.48	14.68 ± 0.31
12:22:57.6618	15:49:25.174	19.34 ± 0.68	18.85 ± 0.81	16.78 ± 0.52	15.17 ± 0.33
12:22:57.4020	15:49:31.175	17.93 ± 0.62	17.92 ± 0.78	15.46 ± 0.49	13.79 ± 0.31
Filament 18,	red diamond				
12:22:58.3898	15:50:57.799	17.51 ± 1.02	17.22 ± 1.27	14.88 ± 0.64	13.21 ± 0.37
12:22:57.8441	15:51: 4.924	19.04 ± 1.22	18.54 ± 1.47	16.33 ± 0.73	14.65 ± 0.43
12:22:57.5323	15:51: 7.924	19.08 ± 1.23	18.84 ± 1.48	17.85 ± 0.86	17.71 ± 0.58
Filament 19,	cyan <i>o</i>				
12:22:59.1169	15:49:19.923	18.53 ± 0.67	18.58 ± 0.83	16.58 ± 0.51	14.97 ± 0.32
12:22:59.0390	15:49:28.173	19.35 ± 0.69	19.36 ± 0.84	16.68 ± 0.48	15.12 ± 0.30
12:22:58.7012	15:49:30.423	17.27 ± 0.57	16.71 ± 0.65	15.18 ± 0.39	13.69 ± 0.25
12:22:58.3634	15:49:35.299	17.71 ± 0.62	17.73 ± 0.76	15.88 ± 0.45	14.22 ± 0.28
12:22:58.1036	15:49:40.174	18.06 ± 0.65	17.77 ± 0.79	15.90 ± 0.48	14.29 ± 0.31
12:22:57.5320	15:49:49.174	19.10 ± 0.71	19.04 ± 0.88	16.82 ± 0.53	15.00 ± 0.34
Filament 20,	blue +				
12:22:58.5970	15:48:40.923	18.14 ± 0.71	17.83 ± 0.84	17.38 ± 0.51	16.32 ± 0.34
12:22:58.3372	15:48:41.299	20.50 ± 0.76	22.50 ± 1.03	16.97 ± 0.47	14.80 ± 0.29
12:22:58.1034	15:48:45.049	19.27 ± 0.68	19.12 ± 0.82	18.55 ± 0.50	16.43 ± 0.31
Filament 21,	magenta <i>o</i>				
12:22:59.5585	15:48:54.797	17.74 ± 0.49	17.44 ± 0.56	15.54 ± 0.27	14.18 ± 0.17
12:22:59.0128	15:48:54.048	17.92 ± 0.52	18.28 ± 0.64	16.08 ± 0.30	14.16 ± 0.18
12:22:58.7790	15:48:55.923	17.85 ± 0.48	17.41 ± 0.54	14.95 ± 0.25	13.25 ± 0.16
12:22:58.5971	15:48:56.673	17.60 ± 0.47	16.87 ± 0.51	15.63 ± 0.27	14.35 ± 0.18
Filament 22,	blue diamond				
12:23: 0.9365	15:50:45.045	18.44 ± 0.95	18.27 ± 1.15	16.17 ± 0.55	14.48 ± 0.34
12:23: 0.8066	15:50:49.545	18.99 ± 1.02	18.68 ± 1.22	17.92 ± 0.67	15.90 ± 0.40
Filament 23,	red <i>x</i>				
12:23: 1.3263	15:50:40.169	17.31 ± 0.82	17.07 ± 0.96	14.86 ± 0.43	13.21 ± 0.26
12:23: 1.3783	15:50:46.544	18.94 ± 0.91	18.62 ± 1.06	16.86 ± 0.51	15.00 ± 0.31
12:23: 1.5083	15:50:49.169	18.27 ± 0.80	17.73 ± 0.91	16.28 ± 0.45	14.54 ± 0.28
Filament 24,	red triangle				
12:23: 1.4819	15:50: 0.419	18.56 ± 0.97	18.45 ± 1.19	15.88 ± 0.67	14.07 ± 0.42

Table 2—Continued

RA	DEC	[3.6] mag	[4.5] mag	[5.8] mag	[8.0] mag
12:23: 1.3520	15:50: 8.294	18.52 ± 0.96	18.21 ± 1.17	16.30 ± 0.69	14.71 ± 0.44
12:23: 1.4821	15:50:21.044	19.38 ± 1.04	19.22 ± 1.28	16.51 ± 0.68	14.75 ± 0.41
Filament 25,	blue x				
12:23: 2.4698	15:50:42.792	18.74 ± 1.10	18.71 ± 1.38	16.51 ± 0.72	15.00 ± 0.44
12:23: 2.5998	15:50:52.917	17.93 ± 1.02	17.83 ± 1.26	15.67 ± 0.62	13.95 ± 0.37
12:23: 2.5999	15:50:58.542	20.25 ± 1.32	20.18 ± 1.62	19.27 ± 0.84	17.10 ± 0.51
12:23: 2.4960	15:51: 3.792	20.05 ± 1.35	20.23 ± 1.71	18.10 ± 0.80	16.27 ± 0.49
12:23: 2.4181	15:51: 8.667	18.58 ± 1.20	18.40 ± 1.47	16.70 ± 0.71	14.91 ± 0.43
Filament 26,	blue triangle				
12:23: 2.6245	15:48:48.417	18.55 ± 0.88	18.29 ± 1.07	16.37 ± 0.56	14.95 ± 0.36
12:23: 2.8324	15:48:50.666	20.51 ± 1.04	19.70 ± 1.23	16.89 ± 0.63	15.29 ± 0.40
12:23: 3.2222	15:48:54.790	19.09 ± 0.98	19.05 ± 1.21	16.76 ± 0.66	15.30 ± 0.42
Filament 27,	cyan +				
12:23: 3.7676	15:48:36.039	18.95 ± 1.18	19.18 ± 1.50	16.75 ± 0.85	15.28 ± 0.55
12:23: 4.0795	15:48:45.413	18.13 ± 1.02	18.03 ± 1.25	16.66 ± 0.76	15.32 ± 0.50
12:23: 4.3654	15:48:51.038	18.72 ± 1.07	18.10 ± 1.25	16.15 ± 0.68	14.32 ± 0.42
12:23: 4.5734	15:48:58.162	19.99 ± 1.26	19.39 ± 1.49	17.06 ± 0.79	15.30 ± 0.49

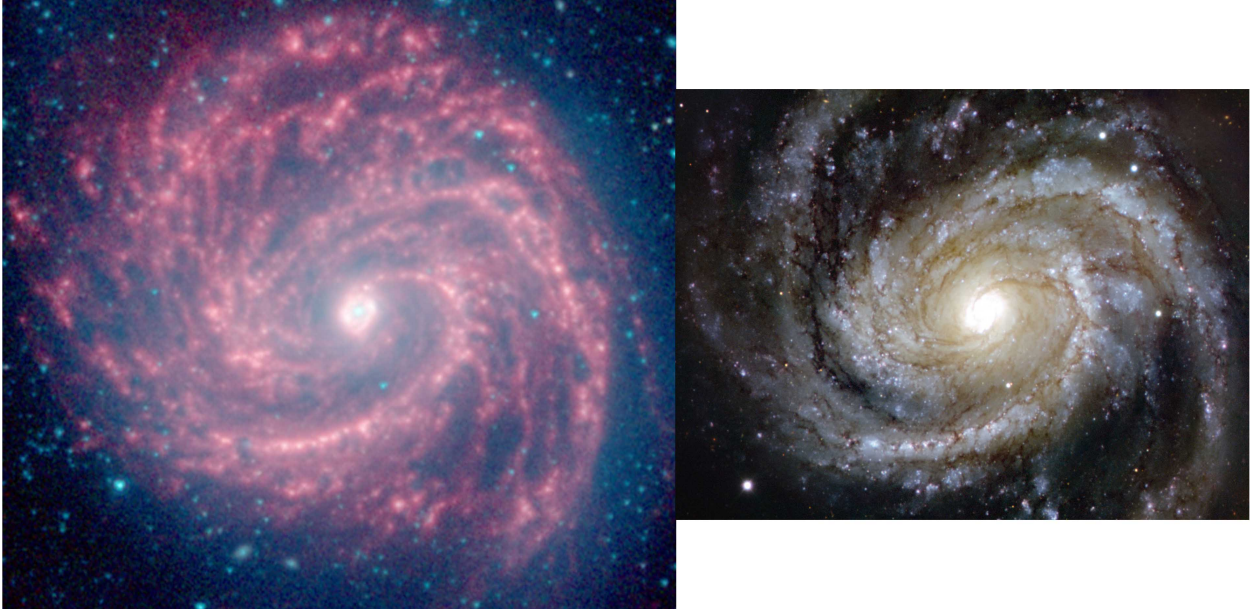


Fig. 1.— Spitzer IRAC image of M100 at $3.6\mu\text{m}$, $4.5\mu\text{m}$, $5.8\mu\text{m}$, and $8\mu\text{m}$ on the left and VLT FORS image in optical bands R, V, and B to the same scale on the right. North is up. The Spitzer image contains many filamentary regions ranging in scale from several kpc in the main spiral arms to hundreds of pc in peripheral regions. The filaments typically contain IR clumps that are spaced apart at approximately equal distances and have similar magnitudes. The IR filaments and the regularity they reveal are not evident in the optical bands, which highlight more the partially obscured HII regions and irregular OB associations.

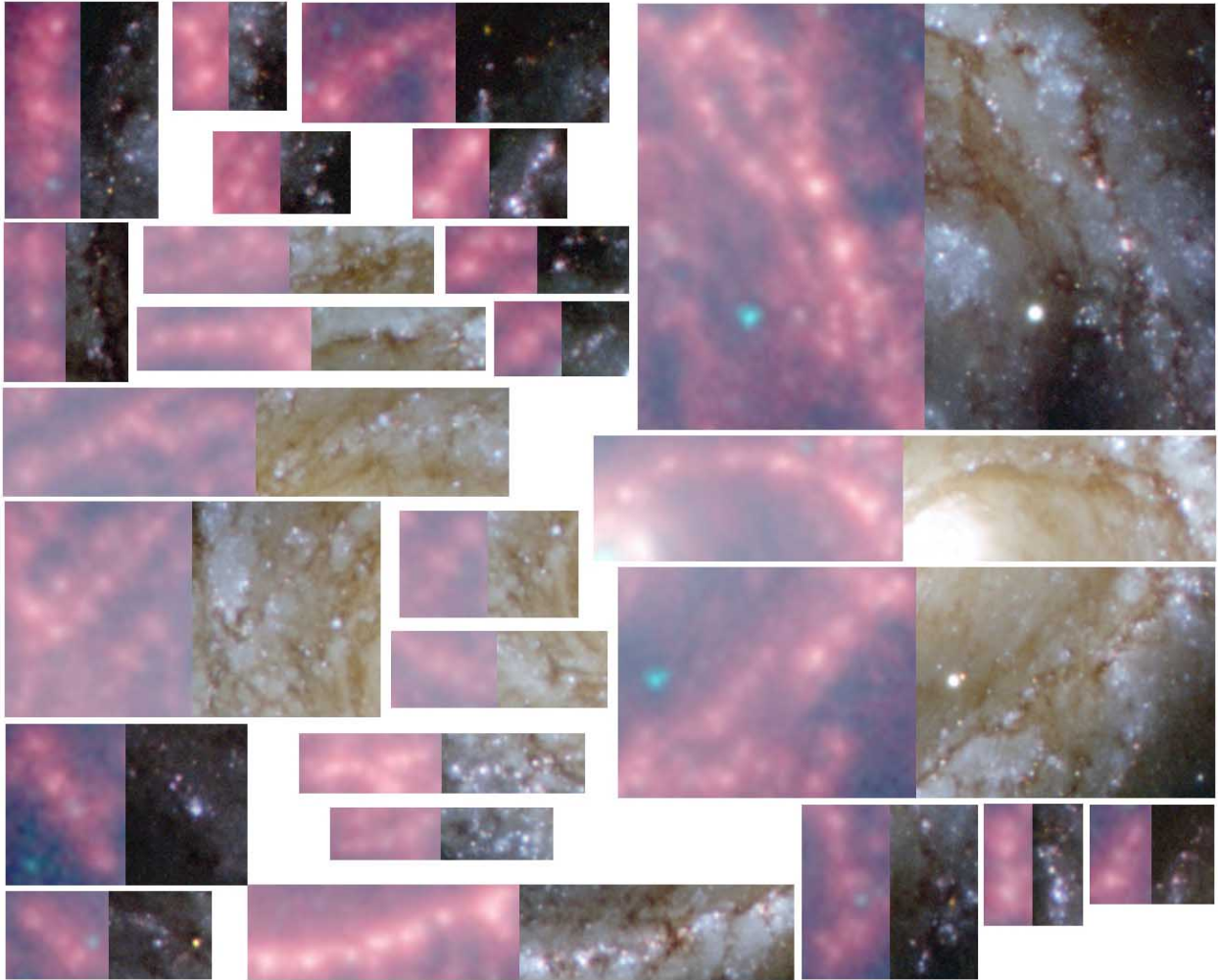


Fig. 2.— Cut-outs from Figure 1 showing clumpy filaments from the Spitzer IR image on the left and the same regions from the VLT optical image on the right. The regularity of the star-forming clumps is clear in the IR images, yet there is often little trace of it in the optical.

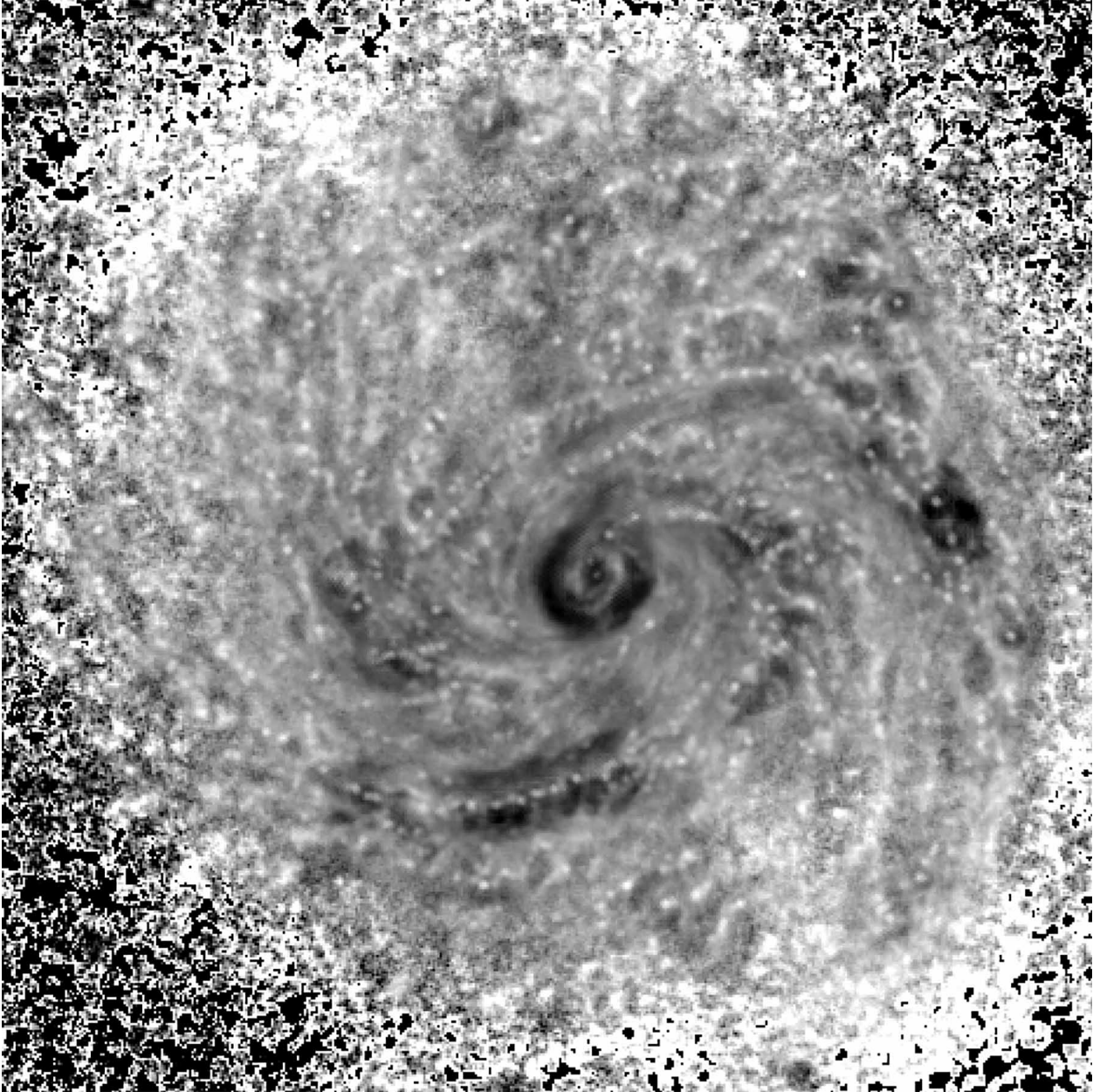


Fig. 3.— IRAC $8\mu\text{m}$ image divided by the MIPS $24\mu\text{m}$ image of M100, plotted on a log scale with the MIPS image multiplied by 4 to match the intensities. The numerous white dots that line up on most of the spiral-like filaments and spurs show the IR clumps studied here. MIPS $24\mu\text{m}$ emission also comes from these clumps, but the angular resolution at $24\mu\text{m}$ is several times larger than the clump size, so the MIPS image provides a good model to divide out the large-scale structure and highlight the $8\mu\text{m}$ clumps. The dark regions around some concentrations of clumps are from the division by broad $24\mu\text{m}$ emission.

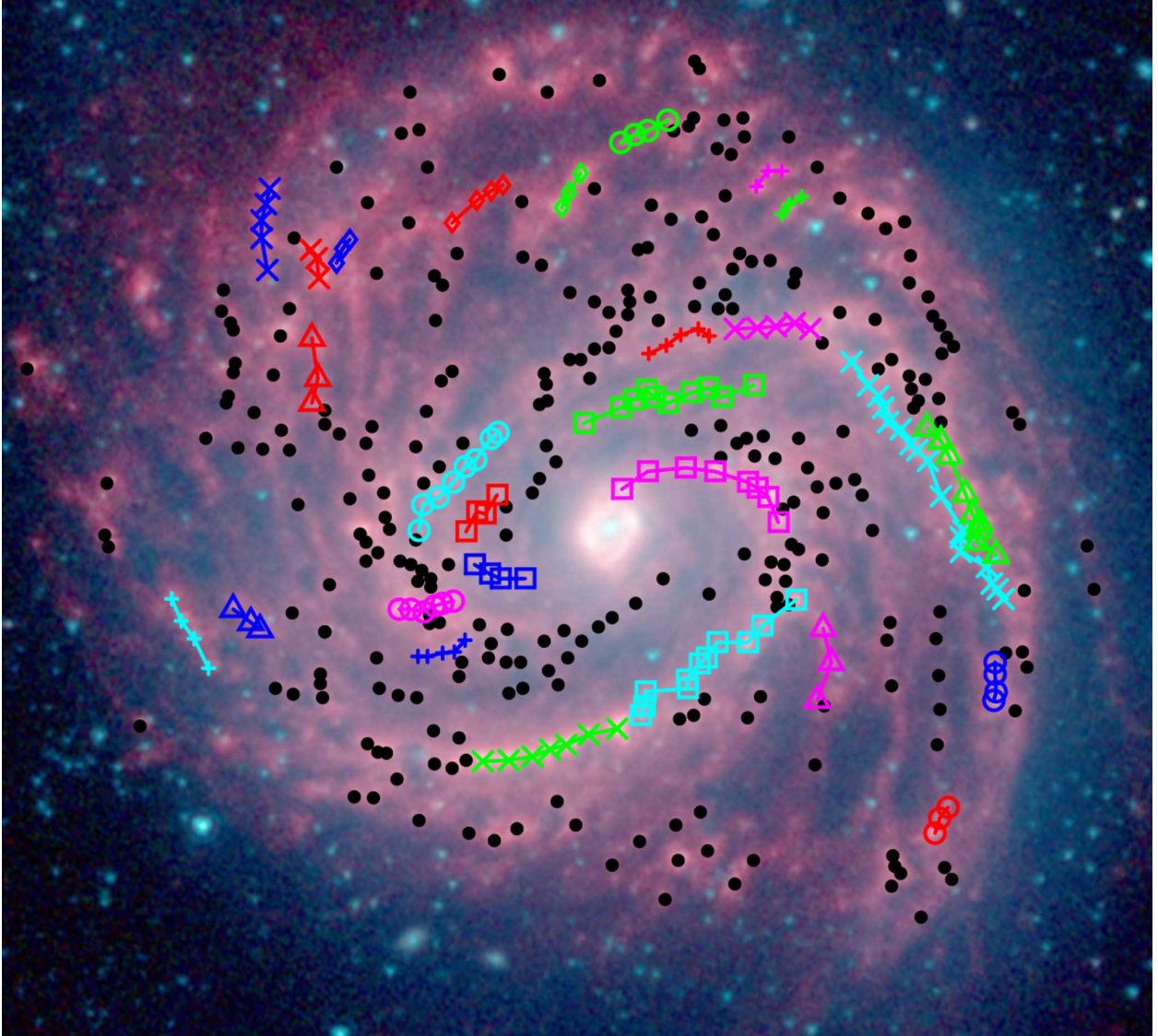


Fig. 4.— The Spitzer image of M100 as in Figure 1 with 422 bright clumps indicated, including 147 with various symbols and colors assigned to 27 distinct filaments, as listed in Tables 1 and 2.

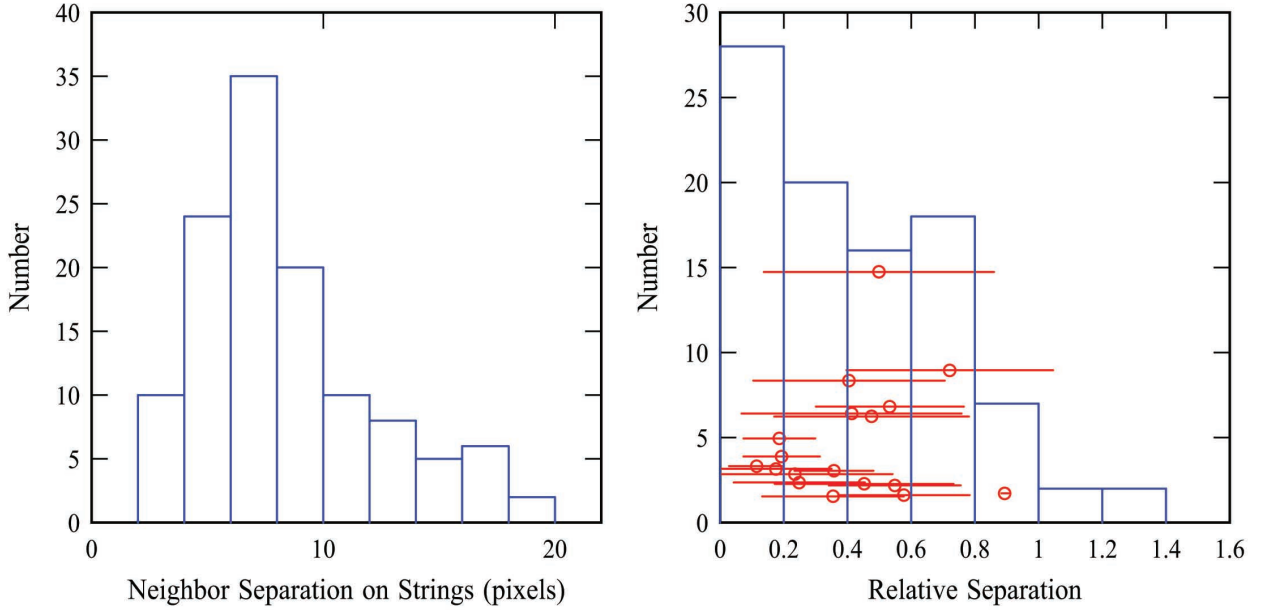


Fig. 5.— (left) Histogram showing the distribution of 120 separations between clumps on the 27 filaments indicated in Figure 4. The separations are measured in pixels on the Spitzer image, which are $0.75''$ and correspond to 60 pc. The peak occurs at 410 pc. (right) Histogram of the relative separations between clumps on the filaments with 3 or more clumps. The relative separation is the difference between two adjacent separations divided by their average separation. The histogram peaks between 0 and 0.2 relative separations, which corresponds to equally spaced clumps, and again between 0.6 and 0.8, which corresponds to a gap between nearby equally-spaced clumps. The circles and horizontal lines are the means and variances of the relative separations for the individual filaments with more than 3 clumps. The circle at $(0.89, 2)$ corresponds to filament 17 with red squares in Figure 4; it has 4 clumps with the inner two close together and the outer two separated by almost the same distance from their adjacent inner clumps, giving a very small variance in the separation differences for each set of 3 contiguous clumps.

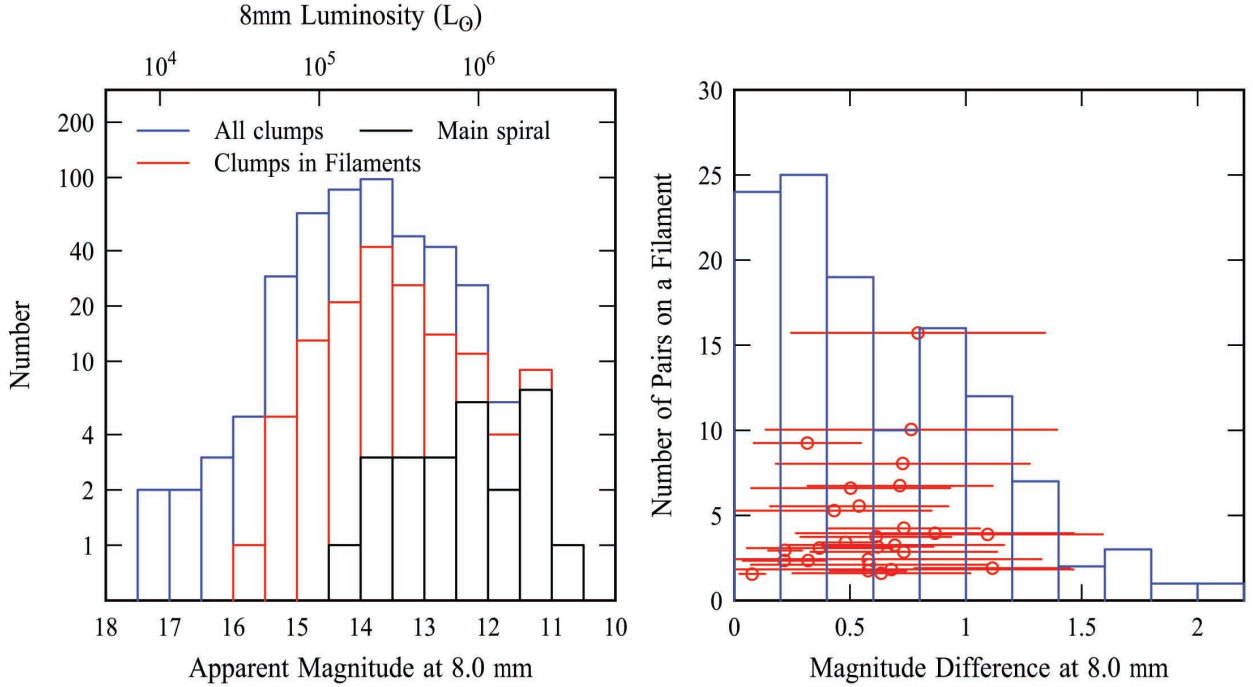


Fig. 6.— (left) Histogram of the apparent magnitude at $8\mu\text{m}$ of all 422 clumps (in blue), all of the 147 clumps in the 27 filaments (red) and the 26 clumps in the main spiral arms (black). The sample is complete to the right of the peak. The luminosity in the $8\mu\text{m}$ band is shown on the top axis. (right) The distribution of magnitude differences between near-neighbor clumps on filaments. Their average difference in magnitudes is only one-third of that expected from randomly sampling the filament distribution on the left, which means that neighboring clumps are more like each other than a random pairing. The circles and horizontal lines are the means and variances of the relative magnitude differences for individual filaments with more than 2 clumps.

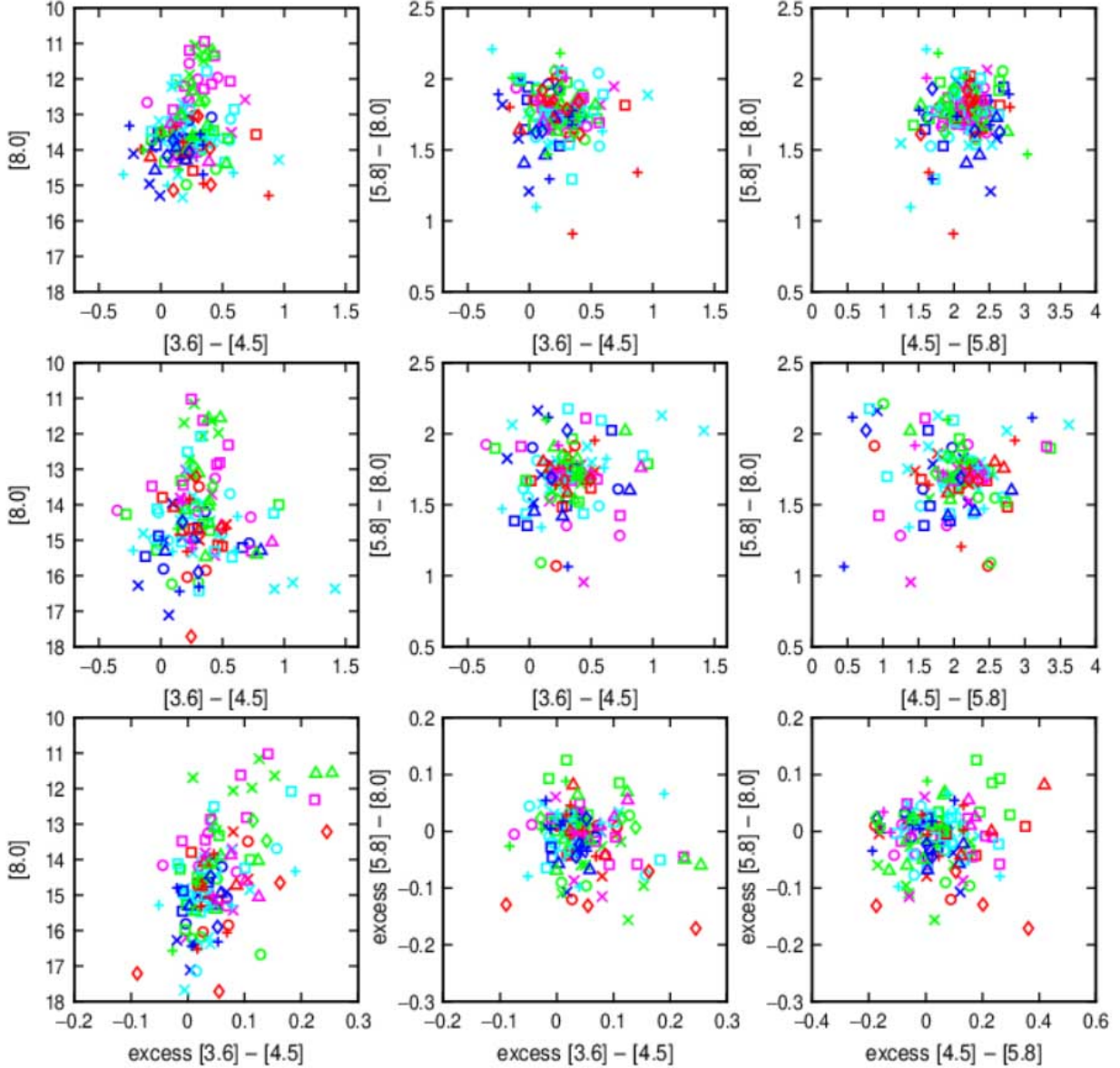


Fig. 7.— Color-magnitude and color-color diagrams of the clumps in the filaments of M100, using the same symbols as in figure 4 to indicate specific filaments. The units on both axes are magnitudes. The top row calculates magnitudes and colors using circular apertures of 2 pixels radius and background subtraction using an annulus from 3 to 4 pixels away from the clump center. The middle row determines the flux from each clump using a circular aperture of 1.5 pixel radius and subtracts a background flux from the underlying filament, taken to be the average of the fluxes in 1.5 pixel radius apertures on each side of the clump, midway to the next clump. The magnitudes and colors of the clumps are calculated from these filament-subtracted fluxes. The bottom row uses the same clump and average-filament fluxes as the middle row, but the colors plotted are the excess colors of the clump compared to the average underlying filament.

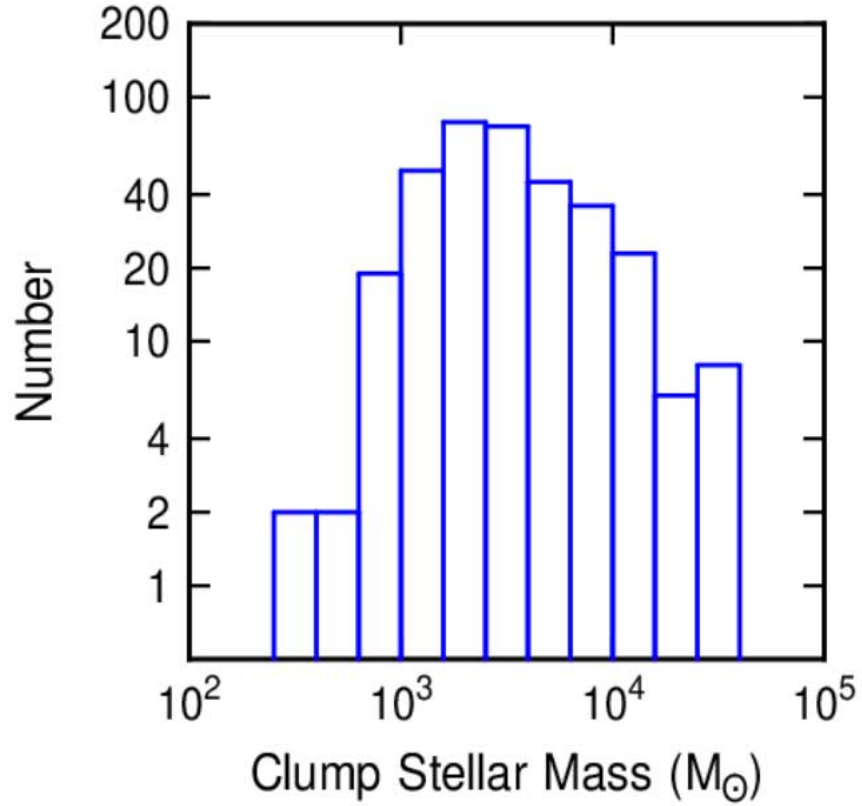


Fig. 8.— Histogram showing the distribution of the equivalent stellar masses for heating of all the measured clumps. The bolometric luminosity is assumed to equal 8 times the sum of the IRAC luminosities, and the associated stellar mass assumes a bolometric magnitude per unit mass equal to -2.7944 , which is appropriate for ages less than 1 Myr. The masses would all be larger by a factor of 5.1 if the ages are 10 Myr.

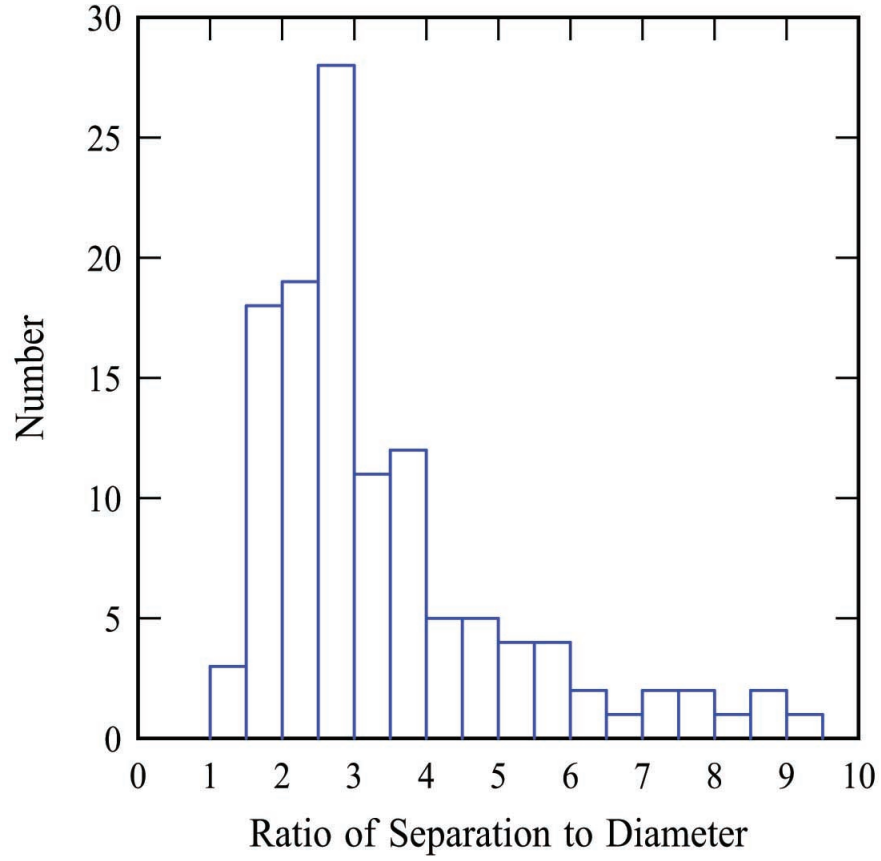


Fig. 9.— Histogram showing the distribution of the ratio of the separation between pairs of clumps to the average diameters of those clumps. The ratio averages approximately 3, which is similar to the value expected from the fastest-growing gravitational instability in a filament with a critical line density.